*minerals*

MDPI

*Article*

# Influence of Low-Temperature Hydrothermal Events and Basement Fault System on Low-Resistivity Shale Reservoirs: A Case Study from the Upper Ordovician to Lower Silurian in the Sichuan Basin, SW China

**Tianqi Zhou [1], Jingshun Cai [2], Shaomin Mou [3], Qun Zhao [1,*], Zhensheng Shi [1], Shasha Sun [1], Wei Guo [1], Jinliang Gao [1], Feng Cheng [1], Hongyan Wang [1], Ling Qi [1] and Pingping Liang [1]**

[1] Research Institute of Petroleum Exploration and Development, PetroChina, Beijing 100083, China
[2] Sichuan Changning Gas Development Co., Ltd., Chengdu 610000, China
[3] China Petroleum Great Wall drilling engineering Co., Ltd., Beijing 100020, China
* Correspondence: zhaoqun@petrochina.com.cn; Tel.: +86-18811588266

**Abstract:** High graphitization is responsible for low-resistivity shale development with poor reservoir quality. This paper provides an explanation of organic matter graphitization and determines the impact of high graphite content on low-resistivity shale reservoir quality at the Wufeng-Longmaxi Formation in the Southern Sichuan Basin. Fine veins are frequently developed at shale samples with Ro > 3.5%, graphitized organic matter > 25%, and resistivity < 5 Ω•m, which are dominated by three mineral assemblages: brunsvigite, barite-hyalophane-barium feldspar-potassium feldspar-anhydrite, and calcite-ankerite. These filling minerals are characterized by an Eu positive anomaly and high Ba, Fe, and Mn contents, suggesting that low-resistivity shale was modified by magmatic-related low-temperature hydrothermal fluid. Temperature measurements of brine inclusions and a semi-empirical geothermometer of chlorite show that low-temperature hydrothermal fluid experienced the chlorite stage (150–180 °C), the low-sulfidation stage (120–150 °C), and the low-temperature calcitization stage. Paleozoic fault systems and late Permian hydrothermal activities associated with the Emeishan mantle plume control the graphitization of low-resistivity shale. The water formation and seawater infiltrated into the deep crust along the Paleozoic basement faults under gravity, developing alkaline hot brine through mantle plume heating and then causing a water-rock reaction with basement rocks. They migrated upward along deep and large Paleozoic faults through convective thermal circulation in the Tiangongtang area, the Shuanglong-Luochang area, and the Xuyong area. Cation exchange and redox reactions occurred during the interaction between high-temperature hydrothermal fluid and cool wall rocks. The migration of alkaline hot brine via the Wufeng-Longmaxi shale introduced a subsequent water-rock reaction, resulting in the development of hydrothermal mineral assemblages that intricately filled fractures. It increased formation temperature and enhanced thermal maturity and graphitization of organic matter at the Wufeng-Longmaxi low-resistivity shale, resulting in a wide distribution of low-resistivity shale at the Changning Block.

**Keywords:** shale gas reservoir; low-resistivity; the Sichuan Basin; graphitization; hydrothermal activity



**Citation:** Zhou, T.; Cai, J.; Mou, S.; Zhao, Q.; Shi, Z.; Sun, S.; Guo, W.; Gao, J.; Cheng, F.; Wang, H.; et al. Influence of Low-Temperature Hydrothermal Events and Basement Fault System on Low-Resistivity Shale Reservoirs: A Case Study from the Upper Ordovician to Lower Silurian in the Sichuan Basin, SW China. *Minerals* **2023**, *13*, 720. https://doi.org/10.3390/min13060720

Academic Editor: Iuliu Bobos

Received: 31 December 2022
Revised: 31 March 2023
Accepted: 21 May 2023
Published: 24 May 2023



## 1. Introduction

Early recognition of low resistivity pay (LRP) (<3 Ω•m) is critical for analyzing its prospects and capabilities [1]. LRP is not confined to specific lithology, which can occur in sandstones, carbonates, and shales associated with a variety of geological events. Scholars have identified five geological events responsible for low-resistivity shale occurrence, including high graphitization of organic matter (OM) [2–4], high Oms and heterogeneous organic-pore structures [5,6], high paramagnetic mineral content, and complicated fault-fracture systems [7,8]. Typically, low-resistivity shale reservoirs are characterized by high

graphite and paramagnetic mineral contents and extremely low resistivity with a value less than 5 Ω•m. This is because the aromatic conjugation of organic matter can rapidly increase at maturity to the over-maturity stage (Ro > 3.5%), where the orderliness and crystallinity of the carbon layer can be dramatically enhanced with a rapid increase in graphite content. The high graphite content in organic matter can result in low electrical resistivity since graphite has a high polarization rate. Currently, scholars have discovered that reservoir quality varies greatly among low-resistivity shale reservoirs, resulting in a significant difference in exploration potential [9,10]. Among the aforementioned influencing elements, graphitization was believed to be the primary cause of poor reservoir quality in over-mature, low-resistivity shale [3,4,11]. Some researchers indicated that, in terms of low-resistivity shales with similar mineral compositions and electrical properties, high graphitized OM content with a value > 25% could result in poor gas generation capacity and storage ability. After graphitization, OM is poor in gas-generating capacity [3,4,12]. Its side chains and heteroatoms can be detached, and thereby, condensation and the directional arrangement of aromatic nuclei can dismantle the mechanical and chemical pore-preservation systems, leading to a significant reduction in OM pores [3,6,13]. Therefore, the governing elements of OM graphitization play a significant role in low-resistivity shale resource exploration and assessment [3,5,11,12]. Previous studies proposed that highly graphitized shale reservoirs could occur under three conditions: they might be buried under 3500 m [5], develop at contact between igneous and metamorphic rock belts caused by global thermal events [2,4,14,15], or develop at contact between rocks with hydrothermal fluids [6,16,17]. The primary controllers of graphitization in various regions need to be further investigated, which will directly influence future exploitation of low-resistivity shale resources.

Numerous black organic-rich shale sequences were deposited at the southern margin of the Sichuan Basin (southern Sichuan Basin), where the Lower Palaeozoic shale (Wufeng-Longmaxi shales) was marked by stable distribution, large thickness, and high quality with enormous resource potential [7]. Previous studies reported that low-resistivity shale in the Southern Sichuan Basin was mainly distributed in 5 regions, including Changning Block, Luzhou Block, Hejiang Block, Zigong Block, and Yuxi Block [7,18–23]. The low-resistivity shale in the Changning Block has the largest scale, with average resistivity generally < 2 Ω•m and highly graphitized OM > 25% [24]. Some studies pointed out that high graphitization was the main controller for the development of low-resistivity shale at the Changning block, and most researchers agreed that the high graphitization of the Changning shale reservoir was primarily related to the eastward emplacement of the late Permian Emeishan large igneous province (ELIP) [25,26]. According to the aforementioned theory, it is difficult to explain why highly graphitized shales are primarily in the west and southeast of the Changning block, while normal-resistivity shales with little graphite are only developed in the center of the Changning block [7].

Hence, primary controllers of graphitization at the low-resistivity Wufeng–Longmaxi shales at the Changning block are essential to be discussed. The Wufeng–Longmaxi shales from four drilling wells at the Changning block are used as an example to examine elements governing graphitization in this study, which focuses on the impact of hydrothermal fluid and fault systems on OM graphitization based on mineralogy and geochemical investigation. It can provide a fresh concept for seeking shale gas targets in future work.

## 2. Geological Setting

The Cathaysia–Yangtze block collision developed the Wufeng–Longmaxi sequences discovered in the Sichuan Basin and its surroundings [21]. The Sichuan Basin and its surroundings were components of the uplift backward unit of the Yangtze foreland basin when the Yangtze plate was a foreland basin after the Middle Ordovician [27,28]. In the Early Silurian, the Sichuan Basin and its perimeter were continually elevated by the intensified southeasterly compression, and the central Sichuan region had an increased paleouplift that exacerbated sedimentary differentiation and reduced water depth [7,29].

During this time, a semi-occluded euxinic basin was created by the Upper Yangtze being positioned between the Leshan paleouplift and the Xuefeng paleouplift. The southern Sichuan Basin, which has an area of 2.2 × $10^4$ $km^2$, is situated at the intersection of the Tethys-Himalayan and Pacific tectonic domains ([30], Figure 1).

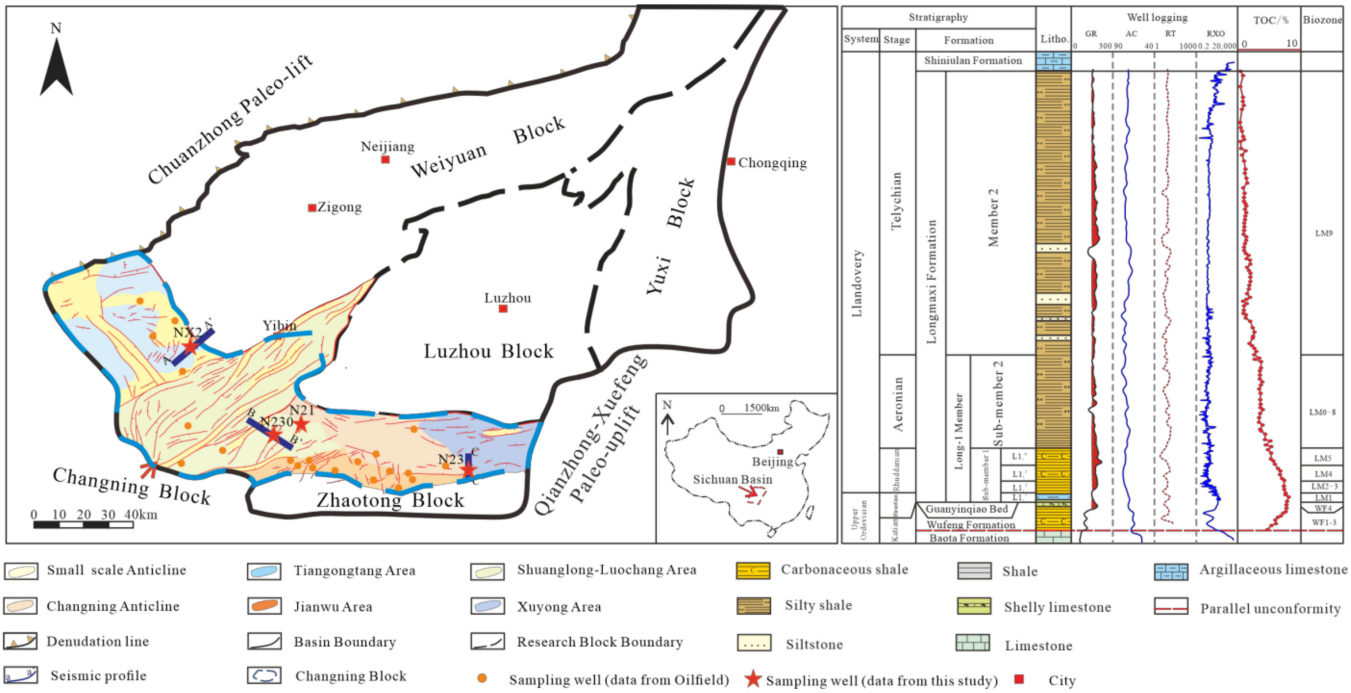


**Figure 1.** Structural position and stratigraphic columnar section of the Southern Sichuan Basin. (**left**) Map showing tectonic sub-units of the Southern Sichuan Basin, with the blue rectangular indications that the location of the Changning Block. (**right**) lithological and stratigraphic figure of the Wufeng–Longmaxi Formation. ((**left**,**right**) modified after [7]).

In the southern Sichuan Basin, the Wufeng Formation may be separated into shale with graptolite belts in the bottom part and Guanyinqiao Member with high limestone concentration at the top, while the Longmaxi Formation can be classified into Long-1 Member (L1) and Long-2 Member (L2) [29]. The L1 member can be divided into the first sub-member ($L1_1$) and the second sub-member ($L1_2$), while the $L1_1$ can be further divided into four layers, e.g., the $L1_1{}^1$ layer, the $L1_1{}^2$ layer, the $L1_1{}^3$ layer, and the $L1_1{}^4$ layer [29]. Meanwhile, the Wufeng Formation is designated as a graptolite belt (WF1-4) [31].

Changning Block is situated southeast of the Sichuan Basin, near the junction of the triangle structural belt at the southern Sichuan Basin and the low-gentle fault-fold belt at the southwestern Sichuan Basin [32]. Folds and faults were extensively formed in this region owing to the Daloushan fault-fold belt and the Daliangshan strike-slip fault belt on the basin's southern boundary [32]. The Changning Block was dominated by a deep shelf environment from the late Ordovician to the Early Silurian, with subaqueous slopes in the north, gravity flow deposits in the west, and subaqueous sub-sags in the center. Low-resistivity shale reservoirs are mostly found in the west (Shuanglong-Luochang area), northwest (Tiangongtang area), and southeast regions (Xuyong area) [33].

## 3. Samples and Methods

A total of 142 Wufeng-Longmaxi shale samples were derived from 4 wells in the Changning Block, with an average resistivity < 10 Ω•m. The NX2 Well and N23 Well are located in the Tiangongtang area and the Xuyong area, respectively. The N30 well and the N21 well are drilled in the Shuanglong-Luochang area. All low-resistivity shale samples in this study are argillaceous shale (Figure 2).

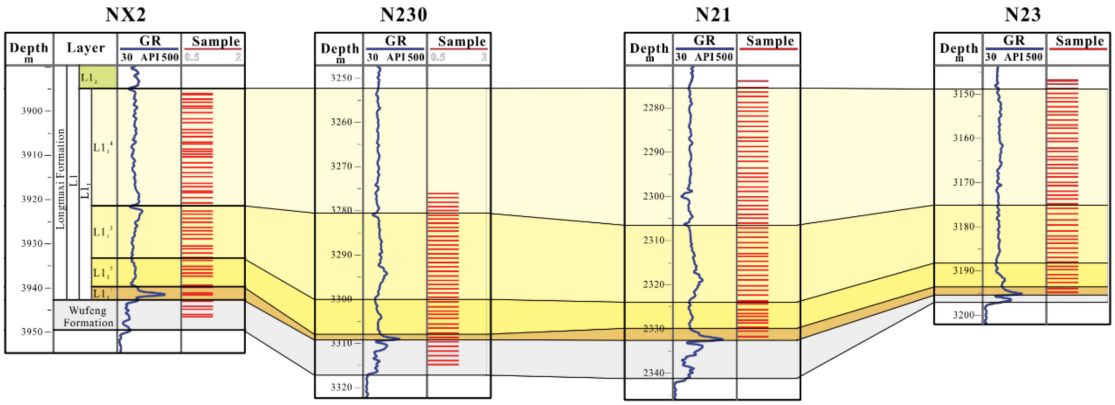


**Figure 2.** Sedimentation section of 4 sampled wells showing the Wufeng–Longmaxi stratigraphic relationship in the Changning Block, the Southern Sichuan Basin.

### *3.1. Mineral Composition and Morphological Analysis*

Using an optical microscope, the mineral distribution and content of 199 thin sections were examined (Leica DM2700p, Leica, Berlin, Germany). Then, using Image J to analyze the images, a quantitative determination of mineral composition and pore types was made.

A total of 199 shale powders underwent X-ray diffraction (XRD), and the clay mineral contents of 104 samples have been measured. At an operating voltage of 50 keV and a current of 800 μA, the X-ray diffractometer Panalytical X-Pert PRO MPD was used to do the test. A rate of 2θ was used to capture diffractograms from 5° to 90°. Following the Chinese oil and gas industry standard (SY/T) 5163-2014, samples were prepared, and spectrum identification was performed [34].

Mineral components, the distribution of OM, and pore shape may all be investigated using a field emission scanning electron microscope (FEI Quanta 650 FEG, FEI, New York, NY, USA) and an energy dispersion spectrometer (EDS, Helios 5 CX, FEI, New York, NY, USA). A total of 20 samples underwent mechanical polishing initially and then 2 h of Arion polishing on Gatan 600 DuoMill equipment (Gatan, New York, NY, USA) at 4 KV and a 7.5° low angle. For more information on milling and SEM observation, see earlier research [29].

#### 3.1.1. Elementary Geochemistry Analysis

The alkali melting glass flakes technique was used to identify the bulk-rock major elements, and the processing and testing of 57 samples were finished at Peking University, Beijing, China. After drying the samples that have been cleaned with deionized water and an ultrasonic wave, use a planetary crusher to reduce the sample's mesh size to less than 200. It was examined using an X-ray fluorescence spectrometer (XRF) built by the Swiss firm ARL, model number ARL-9800. The analytical process follows GB/T14506.28-2010, the Chinese oil and gas industry standard. The element concentration analytical error is less than 5.0%.

The 57 powdered samples were analyzed using an inductively coupled plasma mass spectrometer (ICP-MS) for Rara earth elements. The precise instruments were a PerkinElmer SciexElan 6000, a UV-2600 ultraviolet-visible spectrophotometer, and AA-6800 atomic absorption spectroscopy. The test error was less than 1%. The specific sample handling process in this study followed Zan's steps [35].

Hydrothermal mineral assemblages of 27 samples underwent electron microprobe analyses (EPMA) with a JEOL JXA-8230 electron microprobe with an accelerating voltage of 30 keV and a beam current of 0.01 A. The beam size varied depending on the size of the minerals, from 3 to 5 μm.

Laser ablation inductively coupled plasma mass spectrometry (LA-ICP-MS) at Peking University was used to determine the elemental compositions of chlorite veins from two samples (Beijing, China). LA-ICP-MS is a method that is often used to assess in-situ mineral elemental compositions. It provides the high spatial resolution needed to inves-

tigate the REE element compositions of micrometer-sized scales in situ at various tissue levels [36]. Thermo-Elemental PQ3 ICP-MS with an increased sensitivity S-option interface was used in conjunction with a New Wave Research UP213AI 213 nm aperture imaging laser ablation accessory to complete the analyses. On the conodont element specimens, data were collected for 120 s at each analysis site (spot size of 20 m), taking individual points in different samples [37]. After approximately 60 s of background signal collection, the laser was launched at the sample to capture sample signals for the remaining acquisition time. The obtained REE concentrations were standardized to Sun & McDonough chondrite concentrations [38].

#### 3.1.2. Inorganic Isotope Geochemistry

A total of 14 samples with carbonate veins were chosen for carbon, oxygen, and strontium isotope analyses. The experiment is characterized by the first use of a diamond wire saw to cut along the edge of a calcite vein with a width of 1–2 mm, exposing the calcite vein. Then, using a small dental drill, we carefully collected powder samples from the exposed calcite vein.

In addition, to raise the purity to >99%, samples were powdered to a mesh size of 200 and contaminants (such as quartz particles) were taken out. The samples were broken down using the traditional phosphoric acid procedure at 72 °C, and the chromatographic temperature was 40 °C. Using the V-PDB standard, isotope ratios were determined using a MAT252 mass spectrometer. The data precision is greater than ± 0.1‰.

For Sr isotope analysis, calcite veins also need to be carefully extracted with a dental drill and diamond wire pitch. Ion chromatography was used to extract the pure Sr from the sample after it had been dissolved in HF and $HClO_4$. The MAT-261 mass spectrometer was used to calculate the Sr isotope ratios, which were then adjusted for mass fractionation to get a value of $^{86}Sr/^{88}Sr = 0.1194$. According to the NBS987 standard, the average $^{87}Sr/^{86}Sr$ ratio was 0.710251 ± 0.000009 (2σ, n = 5). The analytical accuracy is <0.004%, and the total Sr procedure blank was less than 0.5 ng.

### *3.2. Organic Geochemistry Analysis*

All powdered samples with grain sizes between 200 and 400 mesh were measured for total organic carbon (TOC) using a LECO CS-200 carbon/sulfur analyzer. The powdered samples underwent treatment with a hydrochloric acid (HCl) solution with a volume ratio of 1:7 for HCl to water. This step aimed to remove any carbonate minerals present in the samples, which can potentially interfere with the measurement of organic carbon content. After the removal of carbonate minerals, the remaining sample was neutralized using distilled water. Subsequently, the residue was dried and then subjected to combustion in order to determine the organic carbon content.

Furthermore, to create pellets of 10 mm × 10 mm × 3 mm in size from shale samples, they were cut parallel to the bedding. Each of the resulting pellets was then meticulously polished with 4000 mesh sandpaper. A total of 48 pellets were selected for measuring the vitrinite reflectance of pyrobitumen using the Raman spectrum. Raman imaging and scanning electron microscopy, developed by Zeiss and WITec, were used together for in situ Raman laser spectroscopy investigations of 928 OMs from 48 samples in order to assess the thermal maturity and the degree of graphitization of OMs found close to hydrothermal veins. In this investigation, a semiconductor laser with a wavelength of 532 nm and a power of 15 MW was employed, together with an energy-dispersive X-ray spectrometer (EDS, Ultim Max65) and a laser Raman spectrometer (Renishaw Company, London, UK, [39]). Since the Wufeng-Longmaxi marine shale is at a high to over-high maturity stage and lacks vitrinite, the equivalent vitrinite reflectance (Ro) was calculated from bitumen reflectance (BRr) using the formula [40]:

$$Ro = (BRr + 0.2443)/1.0495 \quad (1)$$

At least 50 BRrs were observed for each sample on a 3Y microphotometer under reflected light [41].

### *3.3. Electrical Resistivity*

Based on the Petroleum and Natural Gas Industry Standard "SY/T 5385-2007 laboratory measurement and calculation method of resistivity parameters", the resistivity data of 199 shale samples from 4 wells were measured using the pole-pole method. Plungers were drilled with a 25 mm diameter and a length of more than 20 mm, and then they were dried in an incubator for 24 h at 62 °C. The HDTS—II rock resistivity tester was used to measure resistivity at the end [42].

#### 3.3.1. Well logs and Seismic Data

The Changning block's 3D seismic data underwent processing to provide prestack inversion seismic data with a high signal-to-noise ratio and high resolution. With a trace interval of 20 m, the Changning block's seismic exploration area covers 500 square kilometers. The top of the Longmaxi Formation and the bottom of the Wufeng Formation are the two seismic horizons that have been currently interpreted. These seismic horizons in the Changning Block are between 1100 and 2800 m deep. From 4 wells, conventional logs such as gamma-ray (GR), deep and shallow resistivity (RT), bulk density (DEN), true formation resistivity (Rt), and acoustic (AC) logs were collected [43–45].

#### 3.3.2. Fluid Inclusion Analysis

In this research, the petrography and microthermometry of 164 aqueous inclusions were obtained. Among these, 28 samples of barite- and calcite-veined shale samples were made into doubly polished thin sections with thicknesses of around 70 μm. Using a calibrated Linkam THMSG600 heating and cooling stage, which allowed temperature of phase transitions in the range of −196 °C to 600 °C, the homogenization temperature (Th) of 164 aqueous inclusions in barite and calcite veins was determined.

## 4. Results

Evidence from whole rock and micro-in-situ elements, mineralogy, isotopes, and inclusions suggests that fine veins with lengths of about 5–6 mm and widths of 1–2 mm are generally widespread in the low-resistivity shales, whose resistivity is generally lower than 5 Ω•m (FV samples). Different from that, the electrical resistivity of low-resistivity shale without fine veins is generally between 5 Ω•m and 15 Ω•m (NFV samples, Figures 3–5).

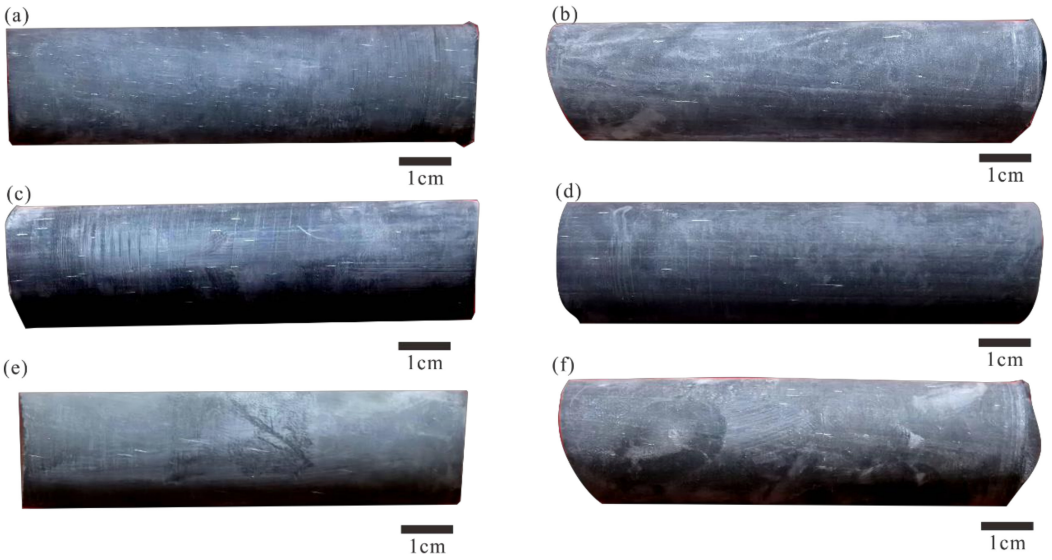


**Figure 3.** Core photos of low-resistivity shale samples with hydrothermal veins. (**a**) Massive argillaceous shale, Well N21, 2328.4 m, 8.02 Ω•m. (**b**) Massive argillaceous shale, Well N21, 2336.94 m, 6.57 Ω•m. (**c**) Siliceous-argillaceous mixed shale, Well N21, 2338.09 m, 4.70 Ω•m. (**d**) Siliceous-argillaceous mixed shale, Well N23, 3163.99 m, 3.31 Ω•m. (**e**) Silty shale, Well NX2, 3928.86 m, 5.948 Ω•m. (**f**) Silty shale, Well N230, 3276.13 m, 4.59 Ω•m.

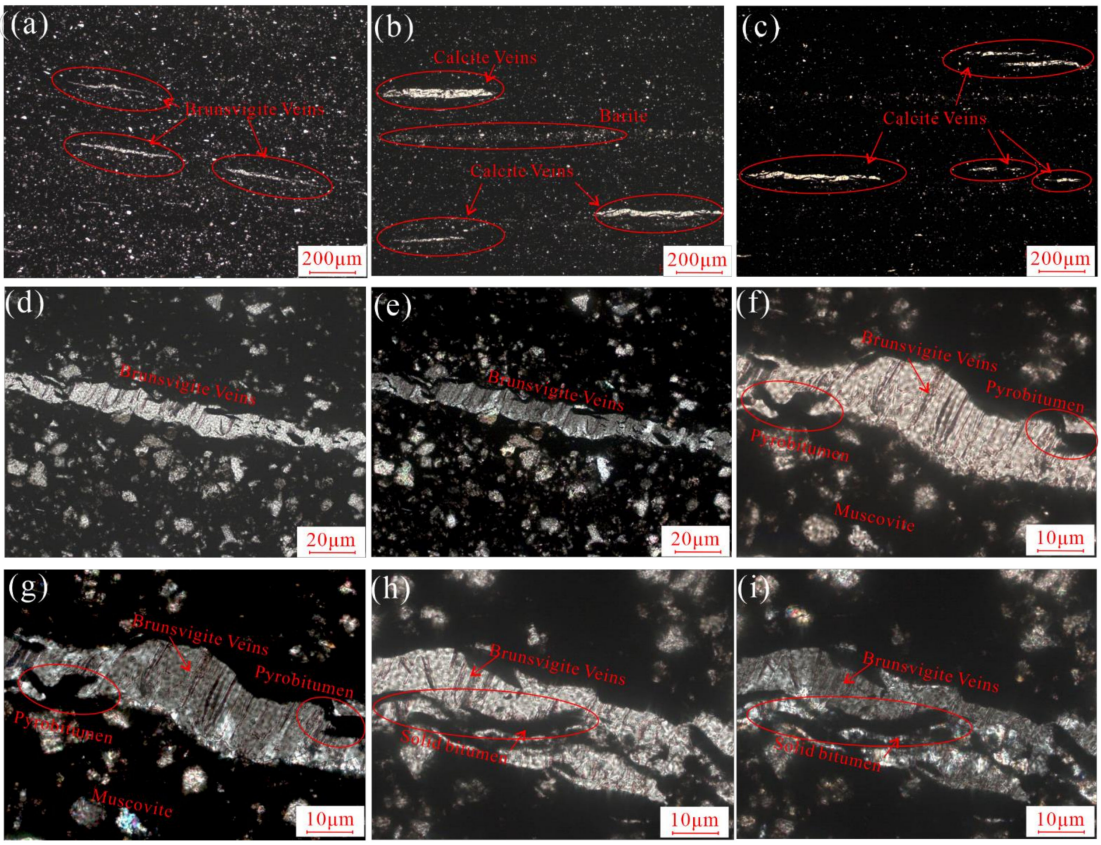


**Figure 4.** Thin-sections of low-resistivity shale samples with hydrothermal veins. (**a**) Brunsvigite veins in massive argillaceous shale, plane polarized light, Well N21, 2328.4 m, 8.02 Ω•m. (**b**) Calcite veins and barite veins in the massive argillaceous shale, plane polarized light, Well N21, 2336.94 m, 6.57 Ω•m. (**c**) Calcite veins in siliceous-argillaceous mixed shale, perpendicular polarized light, Well N23, 3163.99 m, 3.31 Ω•m. (**d**) Brunsvigite veins in siliceous-argillaceous mixed shale, plane polarized light, Well N23, 3163.99 m, 3.31 Ω•m. (**e**) Brunsvigite veins in siliceous-argillaceous mixed shale, perpendicular polarized light, Well N23, 3163.99 m, 3.31 Ω•m. (**f**) Pyrobitumen trapped at brunsvigite veins in silty shale, plane polarized light, Well NX2, 3928.86 m, 5.948 Ω•m. (**g**) Pyrobitumen trapped at brunsvigite veins with detritic muscovite in silty shale, perpendicular polarized light, Well NX2, 3928.86 m, 5.948 Ω•m. (**h**) Solid bitumen trapped by brunsvigite in silty shale, plane polarized light, Well N230, 3276.13 m, 4.59 Ω•m. (**i**) Solid bitumen trapped by brunsvigite in silty shale, perpendicular polarized light, Well N230, 3276.13 m, 4.59 Ω•m.

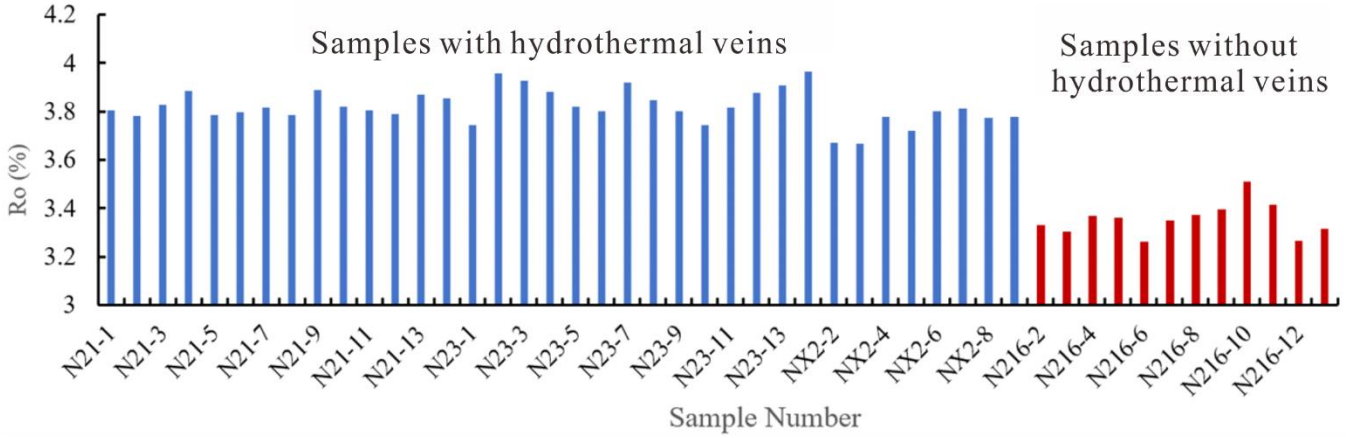


**Figure 5.** Comparison of equivalent vitrinite reflectance (Ro) values of 29 samples without hydrothermal veins and 19 samples with hydrothermal veins.

### *4.1. Lithology*

The difference in lithology between FV samples and NFV samples was described based on mineral composition, TOC content, and major element composition.

#### 4.1.1. Petrography and Mineralogy

The FV samples are dominated by argillaceous shale and siliceous-argillaceous mixed shale, with obvious laminated structure and horizontal bedding. These samples are characterized by high clay mineral contents and carbonate mineral contents. The quartz content is in a range of 6.0%–82.3% (average: 45.3%). Clay content ranges from 1.5% to 55.2%, with an average content of 44.2%. Carbonate minerals are dominated by dolomite and calcite, whose average contents are 14.3% and 32.4%, respectively. TOC contents are in a range of 1.23%–6.18 % (average: 3.76%).

The NFV shale samples are extremely heterogeneous in lithology, which is mainly siliceous-argillaceous mixed shale, with siliceous shale, and silty shale with argillaceous shale of secondary importance. The laminae observed in NFV samples are comprised of alternated dolomite and silty-carbonaceous shale, varying greatly in thickness in a single layer. The NFV samples are high in quartz content and low in clay mineral content compared with the FV samples. The quartz content varies between 6.0% and 82.3%, with an average of 45.3%. The clay content is between 1.3% and 33.3%, with an average content of 23.4%. The carbonate mineral content ranges from 0.2% to 14.2%. TOC varies between 0.76% and 6.32% (average: 2.71%).

#### 4.1.2. Major Elements

In terms of NFV samples, average $SiO_2$ and $Al_2O_3$ contents are 65.94 wt% and 10.29 wt%, respectively, whereas they are 54.20 wt% and 12.22 wt% for FV samples. Importantly, FV samples are richer in MnO and FeO compared with NFV samples. The average MnO and FeO contents of the FV samples are 0.09 wt% and 3.17 wt%, respectively. Fe and Mn enrichment in siliceous rocks is commonly related to hydrothermal activities. Al-Mn-Fe triangle diagram and Fe/Ti-Al/(Al+Fe) cross plot can be used to directly identify siliceous rock origin ([16]).

### *4.2. Organic Matter Graphitization*

The equivalent vitrinite reflectance (Ro) of organic matter in low-resistivity shale was measured in situ by using the Raman imaging and scanning electron microscopy (RISE) system. Measured Ro values vary greatly between FV samples and NFV samples, with average values of 3.75% and 3.47%, respectively. Our previous research has discovered that highly graphitized organic matter frequently occurs in shales with high thermal maturity. Hydrothermal alteration can exert a significant impact on the thermal maturation and graphitization of organic matter. In this study, laser Raman spectra of 928 organic matter samples were collected from 48 low-resistivity shale samples from 4 wells, and the Ro values of each sample were averaged using at least 15 points. Hydrothermal veins are well developed in shale samples from wells N21, N23, and NX2. The Ro values of 7 samples from Well N21 range from 3.74% to 3.96%, while the values of 7 samples from Well N23 and 4 samples from Well NX2 are 3.68%–3.98% and 3.63%–3.80%, respectively. The hydrothermal veins in shale samples from Well N216 are poorly developed, and the Ro values of six samples are in a range of 3.26%–3.51%. Specifically, low-resistivity shale samples with Ro > 3.5% are commonly characterized by highly graphitized OM contents (>25%) [7]. Based on the determined Ro values of the two sample types, it is expected that the graphitization of organic matter in the FV samples is more obvious than that in the NFV samples (Figure 5).

Graphitization in shale rocks has been described by many scholars based on peak intensity ratios of the G-band and D-band, commonly known as Dh/Gh values. A total of 272 organic matter samples from Well N21 were examined, with observed Dh/Gh values ranging from 1.08 to 1.16. Similarly, Dh/Gh values determined from 265 organic matters

from Well N23 are in a range of 0.82–1.14, and Dh/Gh values from 228 organic matter in Well NX2 are between 0.52 and 0.74. Meanwhile, Dh/Gh values of 163 organic matter from Well N216 were calculated, ranging from 0.44 to 0.72 (Figure 6).

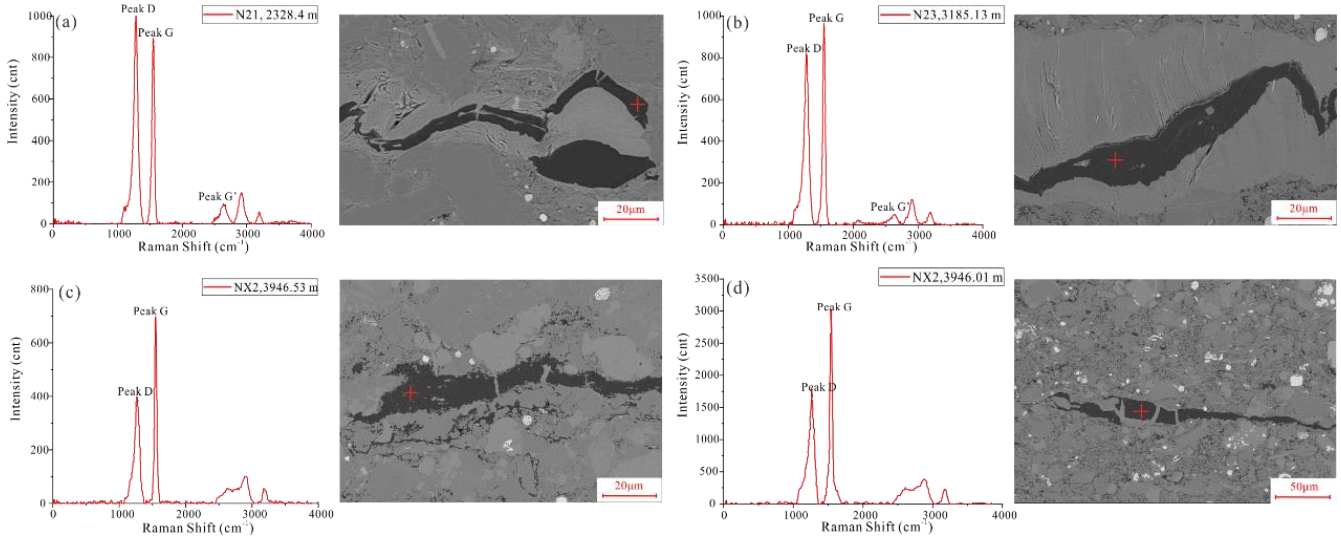


**Figure 6.** BSE images and Raman spectra of low-resistivity shales from the RISE system. Comparison of equivalent vitrinite reflectance (Ro) of 29 samples without hydrothermal veins and 19 samples with hydrothermal veins. (**a**) Graphited graptolite fragments, Well N21, 2328.4 m, Dh/Gh: 1.12, Ro: 3.92%, resistivity: 1.69 Ω•m. (**b**) Solid kerogen with high graphitization, Well N23, 3185.13 m, Dh/Gh: 0.88, Ro: 3.82%, resistivity: 8.01 Ω•m. (**c**) Organic matter without graphitization, Well NX2, 3946.53 m, Dh/Gh: 0.56, Ro: 3.45%, resistivity: 20.40 Ω•m. (**d**) Slightly-graphited graptolite fragments, Well NX2, 3946.01 m, Dh/Gh: 0.59, Ro: 3.49%, resistivity: 17.49 Ω•m.

### *4.3. Hydrothermal Circulation Evidences*

The analysis above suggests that the resistivity of the FV samples is generally lower than 5 Ω•m and may be affected by small-scale hydrothermal reformation at a later stage. Therefore, this study focuses on the relationship between the electrical properties of FV samples and hydrothermal activities. The fine veins in FV samples were sampled for XRD testing, scanning electron microscope observation, and electron probe analyses. The measurement suggests that the veins are mainly filled by three mineral assemblages: brunsvigite, potassium feldspar, hyalophane, barite, and multistage calcite, followed by anhydrite, potassium feldspar, and barium feldspar. These hydrothermal mineral assemblages indicate that the development of the FV samples in Changning Block may be related to hydrothermal activities at a later stage.

#### 4.3.1. Mineralogy

Most veins of the FV samples are dominated by chlorite, occurring within chlorite stacks (Figure 7a–c). Some chlorite vein margins are cemented by barite, barium feldspar, and hyalophane in a poikilitic pattern with blurred mineral boundaries. These minerals obviously coexist with each other under a scanning electron microscope (Figure 7a–c). The chlorite in the FV sample is commonly associated with potassium feldspar. The samples with well-developed chlorite are typically rich in potassium feldspar (Figure 7a–c). Among them, long-strip solid kerogen and amorphous asphalt are often wrapped by chlorite veins (Figure 7a–c). Most solid kerogen is composed of graptolite fragments, radiolarian fragments, and microsomes, while asphalt is dominated by pyrobitumen. Meanwhile, the organic matter surrounded by chlorite veins generally has no organic pores (Figure 7b).

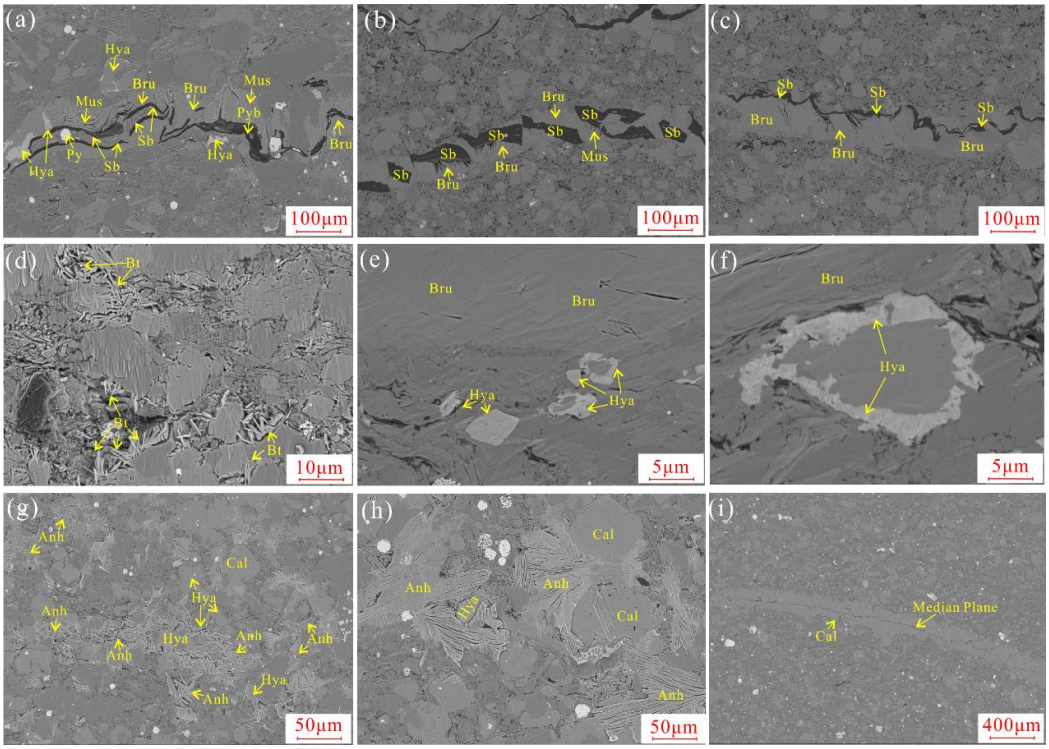


**Figure 7.** FE-SEM images of hydrothermal minerals in low-resistivity shales in the Changning Block. (**a**) Organic matter is wrapped by brunsvigite-hyalophane vein, BSE Image, Well N21, 2328.4 m, 8.02 Ω•m. (**b**) Several solid bitumen segments of are trapped in the brunsvigite vein, BSE Image, Well N21, 2336.94 m, 6.57 Ω•m. (**c**) Graptolite fragments developing in the brunsvigite vein, BSE Image, Well N23, 3163.99 m, 3.31 Ω•m. (**d**) Dendriform, needle-like barite in veins, BSE Image, Well N23, 3168 m, 2.43 Ω•m. (**e**) Massive hyalophane growing near a hydrothermal vein, BSE Image, Well N23, 3167.15 m, 1.83 Ω•m. (**f**) Zonal texture of massive hyalophane, BSE Image, Well NX2, 3928.86 m, 5.948 Ω•m. (**g**) Dendriform, needle-like anhydrite in veins with calcite, BSE Image, Well NX2, 3928.86 m, 5.948 Ω•m. (**h**) Local details of dendriform, needle-like anhydrite around hydrothermal veins, Well NX2, 3930.49m, 5.864 Ω•m. (**i**) Calcite veins in low-resistivity shale, BSE Image, Well N230, 3276.13 m, 4.59 Ω•m. Hya: Hyalophane, Mus: muscovite, Sb: solid bitumen, Pyr: Pyrobitumen, Bru: Brunsvigite, Py: Pyrite, Bt: Barite, Anhydrite: Anh, Cal: Calcite.

Apart from brunsvigite, some veins are composed of barite, hyalophane, and anhydrite (Figure 7d–g). Barite in dendritic-needle shapes under the scanning electron microscope commonly represents amorphous, which has a similar morphology to barite in hydrothermal deposits from the San Francisco Craton [46–54]. The contacts between amorphous barite, barium feldspar, and hyalophane are not clear, occurring as a mixture filling fine veins. Hyalophane occurs as a massive, amorphous pattern filling fine veins. Meanwhile, massive hyalophane often appears around fine veins with zonal structure (Figure 7). In addition, anhydrite (Figure 7g,h) is associated with barite and hyalophane. Different from conventional massive anhydrite, the anhydrite in the FV sample is filled at micro-fractures in crystal clusters and dendritic shapes, which is similar to that in Grimsey hydrothermal fluids in northern Iceland [50].

Calcite-filling fine veins are also widespread in low-resistivity shale samples of the FV samples. Calcite veins are commonly fibrous, reticular, and banded, with a rough surface, incomplete shapes, serrated edges, and obvious dissolution and reformation. In addition, massive ankerite often appears near calcite veins (Figure 7).

#### 4.3.2. Geochemistry

Figure 8 confirms that the NFV samples were fundamentally independent of hydrothermal fluids, while the FV samples may be slightly influenced by hydrothermal fluids

(Figure 8). EPMA findings of chlorite veins reveal that their $Al_2O_3$ and $SiO_2$ contents are in a range of 20.33–22.57 wt% and 28.11–29.61 wt%, respectively. The MgO content varies between 19.85 wt% and 22.97 wt%, and the FeO content varies between 16.28 wt% and 18.68 wt%. The average MnO content might be up to 0.76 wt%.

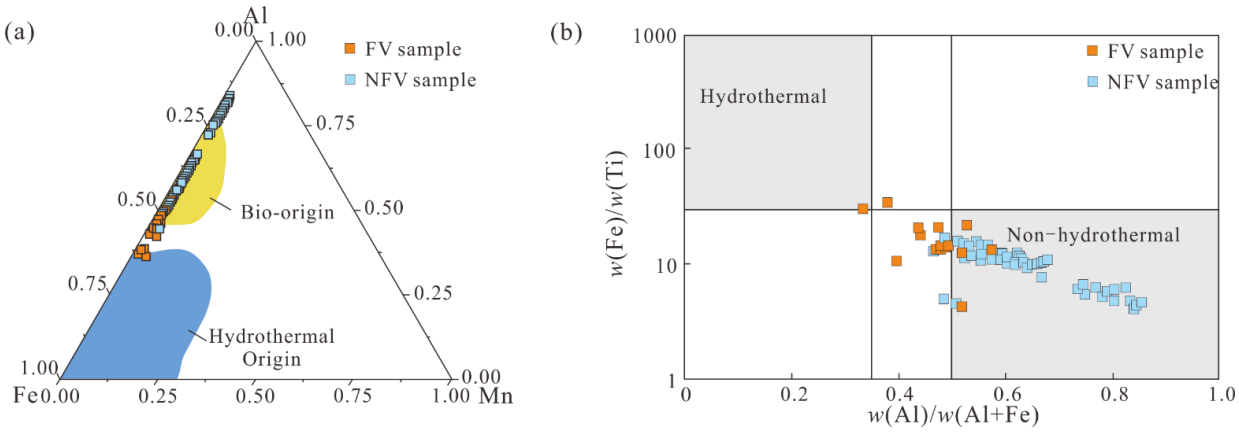


**Figure 8.** Origin of siliceous minerals in two types of Wufeng–Longmaxi low-resistivity shales discussed by (**a**) Al-Fe-Mn triangulation [50] and (**b**) scatter plot of w(Fe)/w(Ti)-w(Al)/w(Al+Fe). Fifteen samples, twenty-two samples, and twenty samples were collected from Well N23, Well N21, and Well NX2, respectively [51].

Chlorite filled in veins is categorized by Zane and Weiss as trioctahedral Mg-Fe chlorite, especially Al-rich Mg-chlorite (Figure 9a,b, [46]), despite the fact that it contains relatively less octahedral Al than that can be further categorized as brunsvigite (Figure 9c). The empirical geothermometer of Kranidiotis and MacLean and the semi-empirical geothermometer were applied to compositional data acquired from chlorite veins [47,48]. The development temperatures of brunsvigite at the FV samples are between 150 °C and 175 °C. A clear difference in chondrite-normalized $REE_N$ patterns can be observed between brunsvigite veins and whole-rock samples (Figure 10). The whole-rock samples from the Wufeng–Longmaxi Formation exhibit right-inclining REE curves, slightly negative Eu anomalies, and REE distributions that are fairly similar to those of the PAAS. The $Eu_N/Eu^*_N$ values of the whole-rock samples range from 0.61 to 0.81 (Eu/Eu* values were calculated using the method described by Taylor [49]). The brunsvigite veins from Well N21, Well NX2, and Well N23, however, show flat $REE_N$ patterns with positive Eu-anomalies, with EuN/Eu*N ranging from 5.46 to 9.10 (Figure 10).

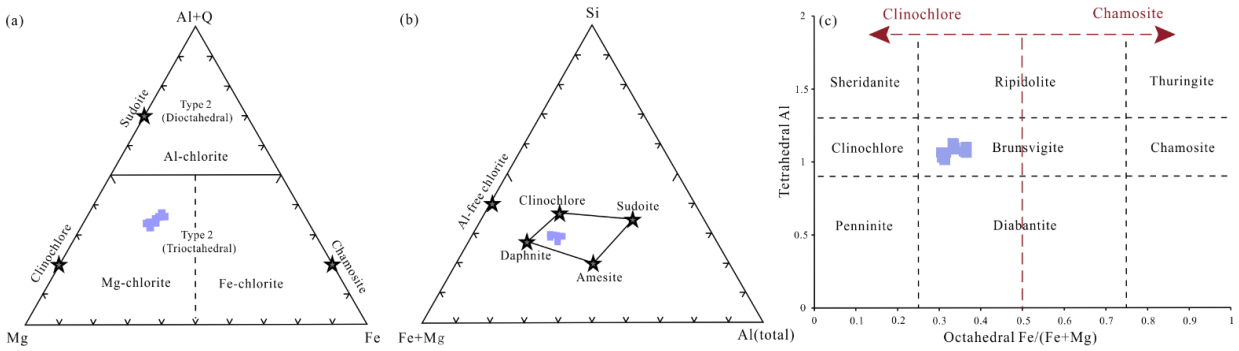


**Figure 9.** Classification of chlorite from the Wufeng-Longmaxi low-resistivity shales at the Changning Block. (**a**) Compositional fields of chlorite (modified by [46]). (**b**) Fe+Mg-Si-Al (total) ternary diagram (modified by [52]). (**c**) Octahedral Fe/(Fe+Mg)-tetrahedral Al binary diagram with various types of Fe-Mg chlorite (modified by [53]). Six samples were from Well N21 (2336.94 m, 2338.09 m, 2339.26 m, 2340.1 m, 2341.27 m, 2342.17 m), three samples were from Well N23 (3166.23 m, 3167.15 m, 3168 m), and one sample was from Well NX2 (3928.86 m).

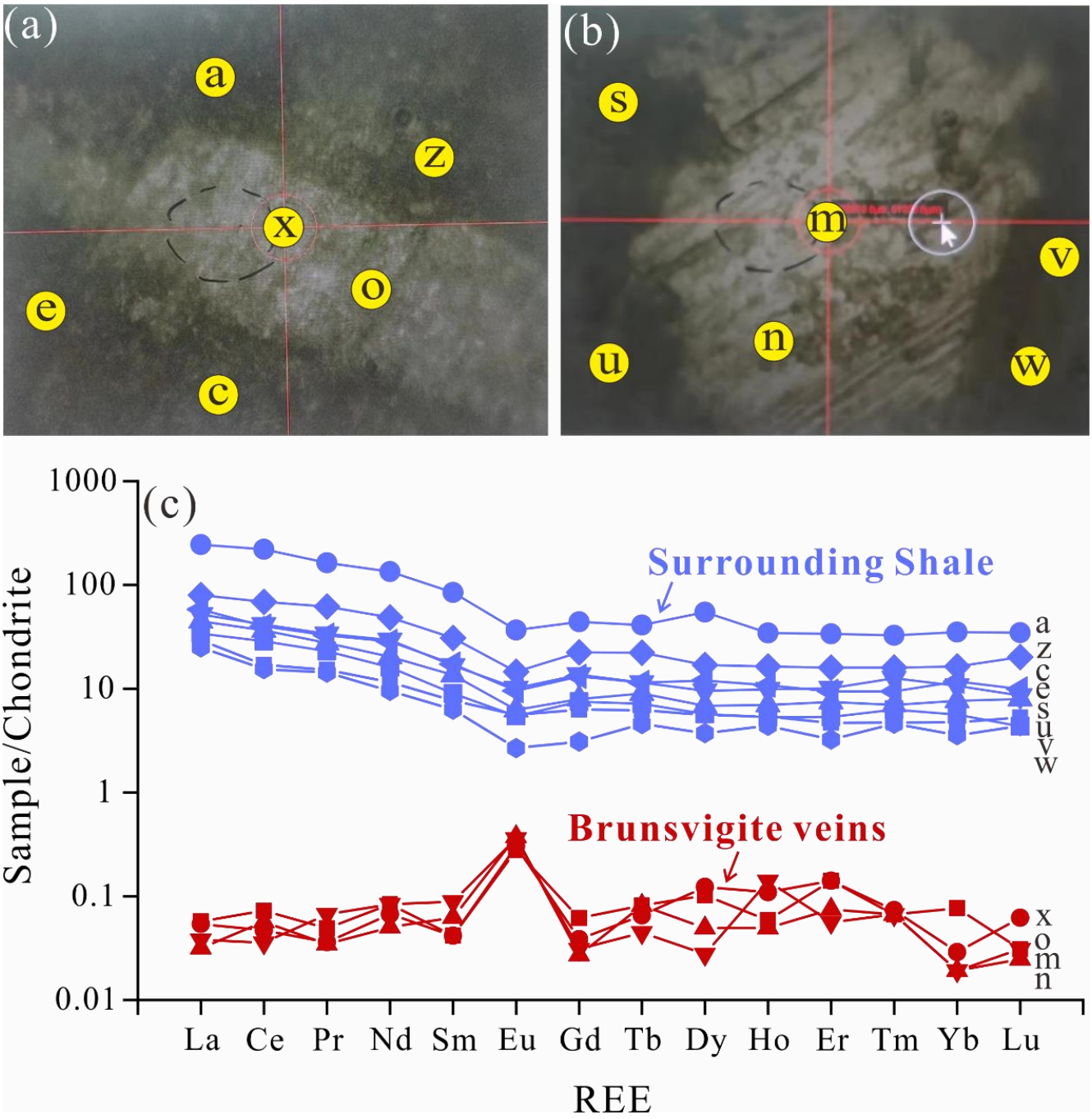


**Figure 10.** Microchemical patterns of brunsvigite veins in the Wufeng-Longmaxi low-resistivity shale. (**a**) Reflected light photomicrograph of the interested brunsvigite grain after laser ablation analyses, Sample 2339.26m, Well N21. (**b**) Reflected light photomicrograph of the interested brunsvigite grain after laser ablation analyses, Sample 3167.15m, Well N23. (**c**) Chondrite-normalized REEN curves of brunsvigite veins derived from microchemical analysis (points a, z, c, e, s, u, v, w) compared with surrounding shale (points x, o, m, n). High REE concentrations in sample 2339.26 m (Well N21, points a, z, x, o, e, and c) are directly correlated with purple colors in figure (**c**). Low REE concentrations (points x, o, m, and n) are correlated with red colors in figure (**c**).

Furthermore, in terms of barite veins from eight samples, BaO contents are about 64.40–65.95 wt%, $SO_2$ contents are 34.28–36.47 wt%, SrO contents are 0.19–0.30 wt%, and $Al_2O_3$ contents are 0.06–0. 21 wt%. Different from that, for massive hyalophane in 19 samples, BaO contents are 12.30–27.80 wt%, $SiO_2$ contents are 42.04–56.62 wt%, $K_2O$ contents are

4.14–9.85 wt%, and $Al_2O_3$ contents are 20.60–23.44 wt%. Meanwhile, the inner zone and outer zone of massive hyalophane are obviously different in components (Figure 11). Taking Sample 2325.88 m in Well N21 for example, the outer zone can be expressed as $K_{0.51}Ba_{0.34}Al_{1.38}Si_{2.65}O_8$, with BaO, $K_2O$, and $SiO_2$ contents of 17.09%, 7.83%, and 52.09%, respectively. The middle zone is $K_{0.55}Ba_{0.24}Al_{1.28}Si_{2.78}O_8$, with BaO, $K_2O$, and $SiO_2$ contents of 12.28%, 8.69%, and 56.62%, respectively. The inner zone is $K_{0.62}Ba_{0.23}Al_{1.20}Si_{2.83}O_8$, with contents of 11.67%, 9.7%, and 56.21%, respectively. It can be seen that the Ba content in the outer zone is higher than that in the core, while the K content in the outer zone is lower than that in the core (Figure 11).

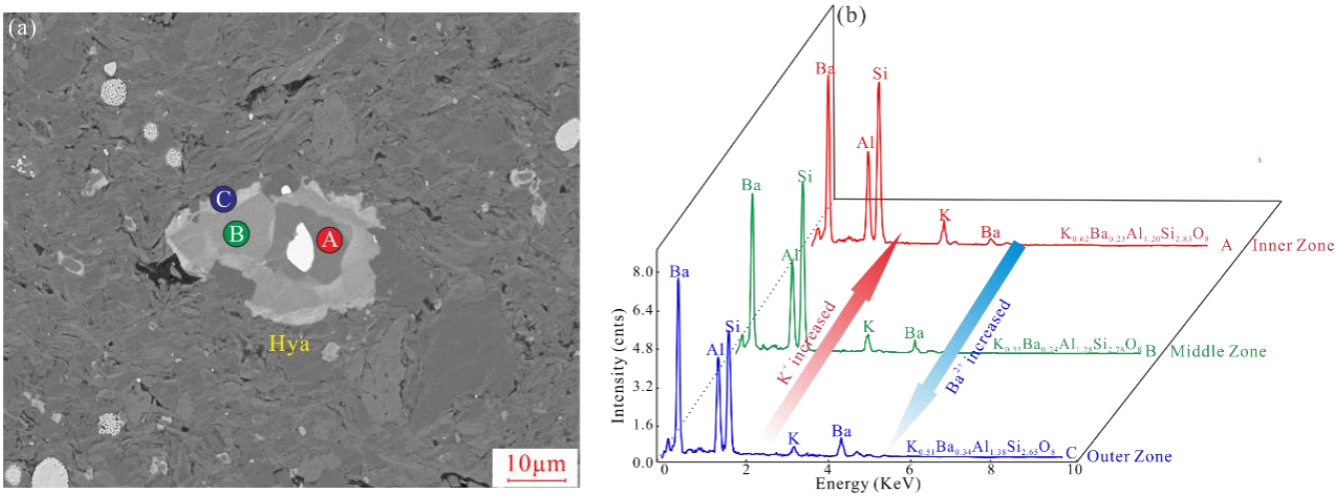


**Figure 11.** Microchemical patterns of massive hyalophane (Hya) with zonal texture. (**a**) BSE image and EPMA data of massive hyalophane with zonal texture, 2325.88 m, Well N21. (**b**) Three EPMA and EDS measurements on hyalophane. The chemical formula of hyalophane was calculated based on EPMA results.

The total rare earth element concentrations of barite and hyalophane veins in 8 samples from Wells N21 and N23 vary from 164.3 ppm to 216.31 ppm, with a median value of 188.27 ppm, higher than the 185 ppm of the PAAS standard (Figure 12). Moreover, barite and hyalophane veins from 8 samples exhibit convex PAAS-normalized $REE_{PAAS}$ patterns with slightly positive Eu anomalies (ranging from 1.71 to 1.83, Figure 12), which is similar with the $REEE_{PAAS}$ patterns of brunsvigite veins, whereby positive Eu anomalies are also observed (Figure 10c).

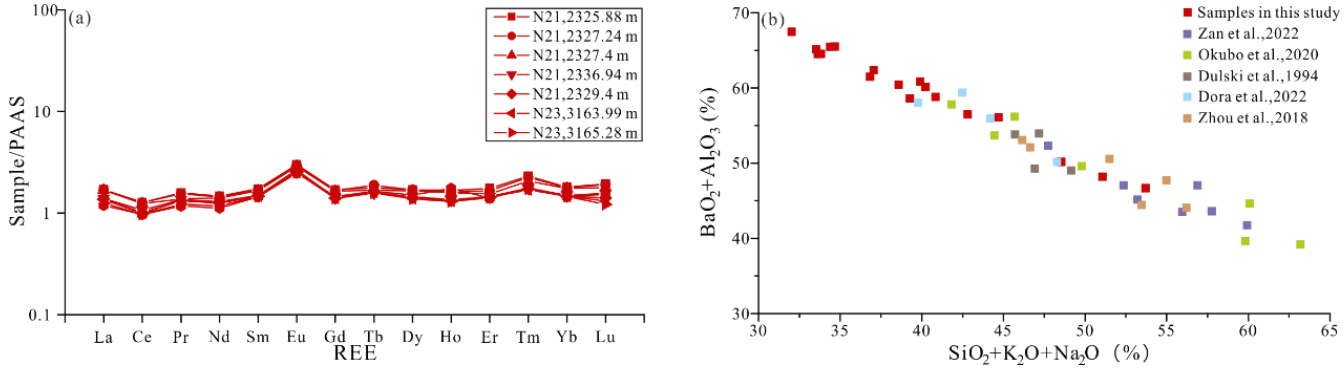


**Figure 12.** Geochemical elements of barite veins and massive hyalophanes in low-resistivity shale reservoirs. (**a**) REE distributions of barite veins in low-resistivity shales. (**b**) Comparison of major element concentrations of hyalophanes among Wufeng–Longmaxi low-resistivity shale and other shale from other areas.

Carbon and oxygen isotopes suggest that calcite veins in the FV samples can be divided into two phases. In terms of Phase I, $\delta^{13}C_{V\text{-}PDB}$ is −0.72‰–−3.17‰, with an average of −1.87‰, and $\delta^{18}O_{V\text{-}PDB}$ is −9.45‰–−6.23‰, with an average of −8.03‰. In terms of Phase II, $\delta^{13}C_{V\text{-}PDB}$ is −10.11‰–−1.45‰, with an average of −4.47‰, and $\delta^{18}O_{V\text{-}PDB}$ is −16.65‰–−7.05‰, with an average of −13.19‰. The electron probe analysis of the calcite veins shows that the major elements of the veins are obviously different from those of the surrounding host rocks. Specifically, surrounding host rocks are mostly composed of $SiO_2$, $Al_2O_3$, FeO, MnO, MgO, and CaO, with average concentrations of 60.60 wt%, 11.17 wt%, 3.24 wt%, 0.06 wt%, 2.43 wt%, and 2.27 wt%, respectively. The hydrothermal calcite veins are dominated by CaO, MgO, FeO, MnO, and $Al_2O_3$, with average concentrations of 54.45 wt%, 0.46 wt%, 0.42 wt%, 0.29 wt%, and 0.26 wt%, respectively (Figure 13c,d).

The difference in Sr isotopes between calcite veins and surrounding host rocks can be used to characterize fluid sources and preservation conditions (Figure 14). The calcite veins of hydrothermal origin in welsl NX2, N23, and N21 are 0.716115–0.721060 in $^{87}Sr/^{86}Sr$ values, while the surrounding host rocks are 0.714118-0.718738 in $^{87}Sr/^{86}Sr$ values. The difference is between 0.001030 and 0.002322, which is much higher than that at the Changning Anticline (Figure 14 [54–57]).

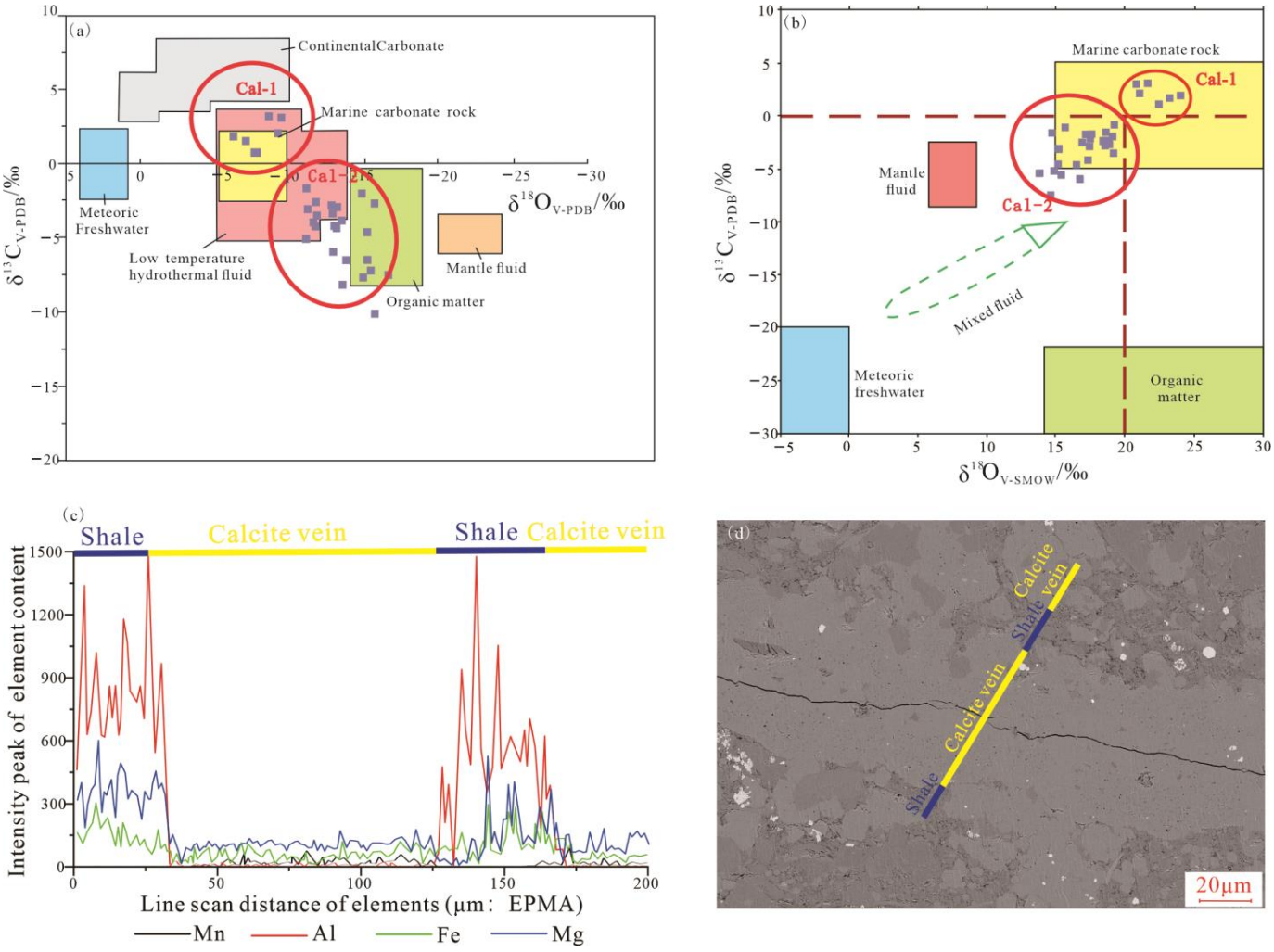


**Figure 13.** Carbon and oxygen isotopic compositions and origins of calcite veins in the low-resistivity shale samples. (**a**) Cross plot of $\delta^{13}C_{V\text{-}PDB}$ vs. $\delta^{18}O_{V\text{-}PDB}$, (**b**) Cross plot of $\delta^{13}C_{V\text{-}PDB}$ vs. $\delta^{18}O_{V\text{-}SMOW}$. Data of continental carbonate, marine carbonate rocks, organic matter, low-temperature hydrothermal fluid, and mantle fluid flow from Wu [56]. (**c**) Peaks represent Mn, Al, Fe, and Mg contents in surrounding shales and calcite veins, respectively. (**d**) BSE image shows the locations of EPMA data points.

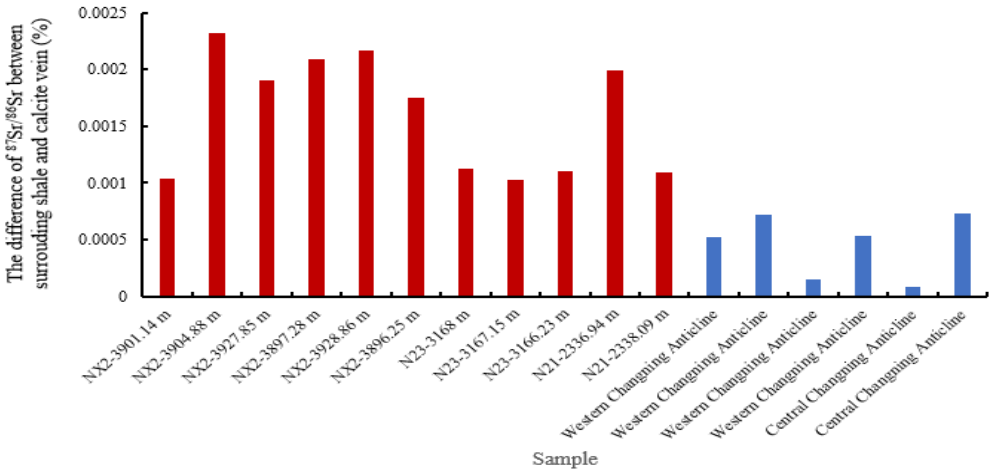


**Figure 14.** Differences in $^{87}Sr/^{86}Sr$ between surrounding shales and calcite veins in Well NX2, Well N23, Well N21, and Changning Anticline. The data for the Changning Anticline was from [57].

#### 4.3.3. Fluid Inclusion

Petrographic and thermometric analyses were carried out on 164 brine inclusions from calcite veins and barite veins related to hydrothermal fluids. Gas–liquid two-phase brine inclusions are widespread in calcite veins and barite veins. The inclusions are mainly elliptical, sub-circular, and irregular in shape, with diameters of 5–15 μm (Figures 15 and 16). Two brine inclusion types are well developed in calcite and barite veins related to hydrothermal activity. The first type is zonally distributed along calcite cleavage. Homogenization temperatures for thirty-three brine inclusions in Well NX2 are 122 °C–150 °C, while they are 101 °C–118 °C for twenty-eight brine inclusions in Well N23. The second type is distributed in clusters. The homogenization temperatures of thirty-two brine inclusions in well NX21 and thirty-seven brine inclusions in well N23 are 84 °C–213 °C and 100 °C~120 °C, respectively (Figures 15 and 16).

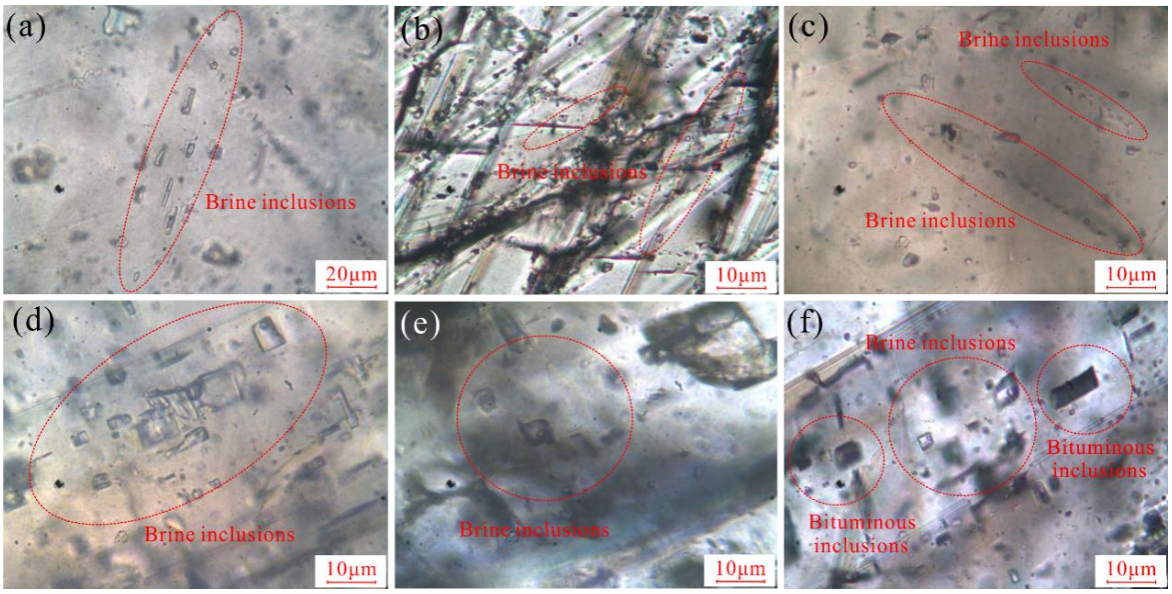


**Figure 15.** Micrographs of inclusions in calcite veins captured under plane-polarized light. (**a**) Gas-liquid two-phase brine inclusions along micro-fractures in calcite veins, Well NX2, 3946.53 m. (**b**) Gas-liquid two-phase brine inclusions along calcite cleavage, Well NX2, 3944.80 m. (**c**) Brine inclusions in micro-fractures in calcite, Well NX2, 3920.77 m. (**d**) Brine inclusions along calcite cleavage, Well N23, 3163.99 m. (**e**) Brine inclusions in clusters, Well N23, 3165.28 m. (**f**) Bituminous inclusions and brine inclusions along calcite cleavage, Well N23, 3168 m.

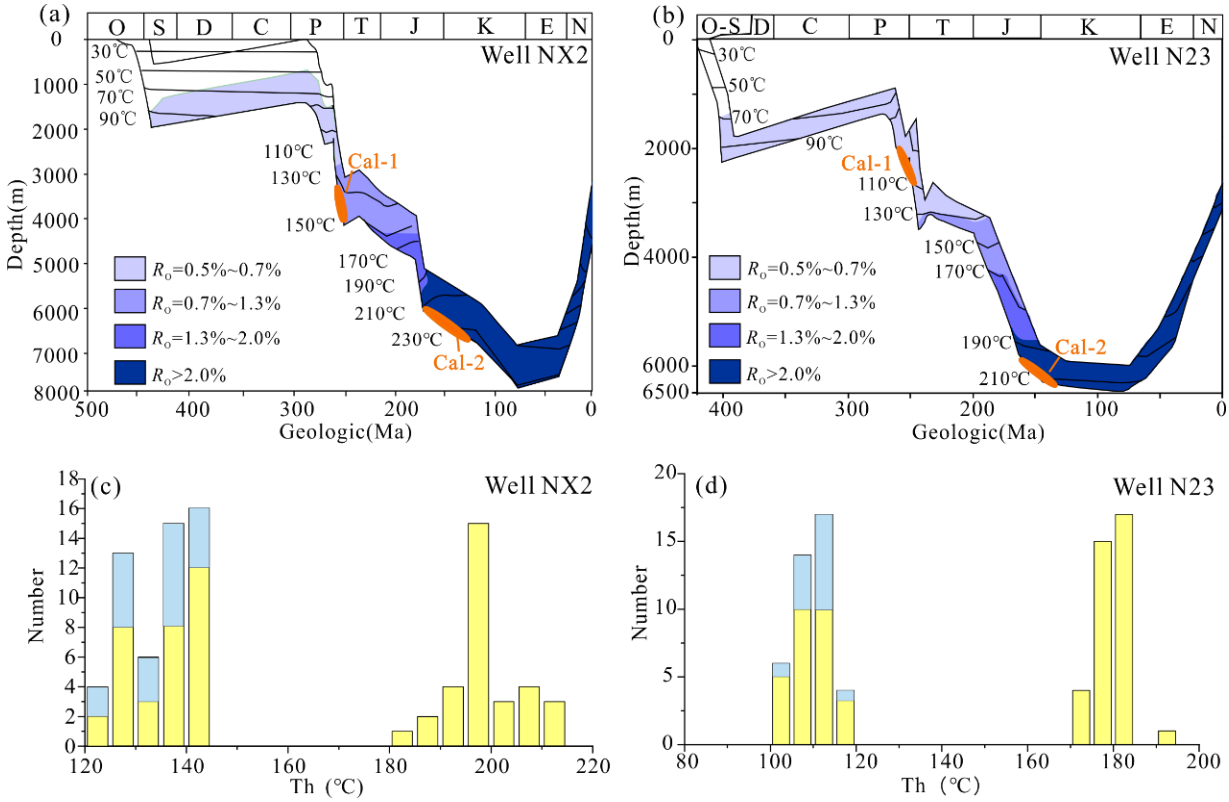


**Figure 16.** Development timing of calcite veins in low-resistivity shales. (**a**,**b**) Thermal-burial histories of the Wufeng–Longmaxi shales in Well NX2 and Well N23, respectively, two calcite-vein stages; thermal-burial histories of two wells modified by [56]. (**c**,**d**) Homogenization temperatures of brine inclusions in calcite veins from Wells NX2 and N23, respectively. Micrographs of inclusions in calcite veins captured under plane-polarized light. (**a**) Gas-liquid two-phase brine inclusions along micro-fractures in calcite veins, Well NX2, 3946.53 m. (**b**) Gas-liquid two-phase brine inclusions along calcite cleavage, Well NX2, 3944.80 m. (**c**) Brine inclusions in micro-fractures in calcite, Well NX2, 3920.77 m. (**d**) Brine inclusions along calcite cleavage, Well N23, 3163.99 m.

### *4.4. Electric Resistivity of Low-Resistivity Shale Rocks*

The Wufeng-Longmaxi low-resistivity shale at the Changning Block varies greatly in resistivity, ranging from 0.18 Ω•m to 47.13 Ω•m. Most NFV samples are developed in the central portion of the Changning Block, with an average resistivity of 12.63 Ω•m, while considerable FV samples are distributed in the Shuanglong-Luochang area, in the western portion of the Changning Block, with an average resistivity of 1.53 Ω•m. FV samples are also occurring in the southeast and northwest of the Changning Block, particularly in the south of the Xuyong area, with an average resistivity of 2.21 Ω•m (Figure 1).

## 5. Discussion

The evidence from petrography and in situ geochemical analysis of mineral assemblages such as brunsvigite, hyalophane, feldspar-barite-potassium, feldspar-anhydrite, and calcite, fault systems, carbon and oxygen isotopes, and homogenization temperature measurement of brine inclusions suggests that the low-resistivity shale in Changning Block is jointly controlled by alkaline hot brine and Paleozoic basement faults at the transition of P-T.

### *5.1. Origin of Hydrothermal Mineral Assemblages*

#### 5.1.1. Chloritization Stage

Chlorite can be greatly varied in its compositions, which are controlled by various factors, e.g., original rock compositions, formation fluids, temperature and pressure, and

oxidation or reduction environments. These variations provide valuable information about fluid composition evolution [58,59]. Different from low-resistivity shale, chlorite is commonly occurring in two forms in the Wufeng–Longmaxi shale reservoirs with an average resistivity > 20 Ω•m. Intergranular pores associated with quartz and feldspar aggregates are filled by nanometer chlorite and other lowly-automorphic clay mineral assemblages. Furthermore, chlorite may also infiltrate normal-resistivity shales by adhering to the surfaces of quartz and feldspar as a coating [55]. Fe is poorly enriched in these chlorites, with a negative Eu anomaly compared with vein chlorite and an average Fe/(Fe+Mg) value of 0.16–0.23.

Compared with normal-resistivity shale reservoirs, low-resistivity shales with average resistivity lower than 5 Ω•m have abundant brunsvigite fine veins and are rich in Al and Mn (Figure 9). Most scholars point out that brunsvigite occurrences are often associated with hydrothermal activities [54,55]. Abundant Mn in Figure 9 is a good indicator of Al-Mn clinochlore. Some studies have found that the high tetrahedral Al content in chlorite represents an environment with high formation temperatures. Since samples are low in tetrahedral Al content, it can be inferred that brunsvigite was likely formed in an environment with relatively low temperatures (Figure 9c). Evidence of cogenetic precipitation of potassium and chlorite at low-resistivity shale reservoirs in the Southern Sichuan Basin strongly supports hydrothermal origin for both phases ([54], Figure 7a–c). Some scholars believe that brunsvigite-muscovite-potassium feldspar often appears in low-sulfidation systems (LSS) [60] that are developed in distal environments from almost neutral and reducing hydrothermal fluids, with brunsvigite as the primary hydrothermal phyllosilicate [54]. Huang found that the brunsvigite in the low-resistivity shale co-existed with fibrous calcite veins in the Sichuan Basin, which could also confirm the occurrence of LSS [54]. However, brunsvigite was not directly derived from the Permian Emeishan alkaline basalt but might be associated with the infiltration of formation water or seawater heated by heat sources from deep basins, which can be confirmed by two pieces of evidence. Firstly, the Permian basalt chlorite in the Sichuan Basin is dominated by ferroan clinochlore, while the brunswigite content is high in the Upper Permian pyroclastic rocks. The Si/Al ratio of brunswigite in our study is 1.08–1.23, which is similar to that of Permian pyroclastic rocks but is obviously lo71wer than that of the ferroan clinochlore in basalt (Si/Al ratio: 1.86–2.41), indicating the brunswigite in low-resistivity shale was not directly originated from basalt. The Si/Al values indicate the brunsvigite was derived from smectite evolution, where the $Fe^{3+}$, $Mn^{2+}$, and $Mg^{2+}$ required in the brunsvigite development might be sourced from deep thermal fluids. Secondly, an obvious positive Eu anomaly occurs in the brunsvigite (Figure 10), indicating a genetic relationship between chlorite and hydrothermal fluids. However, the REE distribution pattern of brunsvigite is different from that of the Upper Permian ELIP in the Sichuan Basin, indicating that the ore-forming materials of brunsvigite are not directly derived from magmatic-hydrothermal fluids [61]. The above analysis suggests that the brunswigite veins in the low-resistivity shale are formed by the water–rock reaction between hydrothermal fluids and shale. Cations in montmorillonite plates in low-resistivity shale are exchanged, where $Ca^{2+}$ and $Na^{+}$ are discharged. $Fe^{2+}$ and $Mg^{2+}$ migrated by hydrothermal fluid can be combined with $OH^{-}$ electrolyzed by water to form brucite-like sheets, entering the montmorillonite plates as octahedral sheets. They can combine in a ratio of 2:1:1 to form brunswigite veins.

#### 5.1.2. Sulfatization Stage

Additionally, brunswigite-mica hydrothermal mineral assemblages, barite, hyalophane, and anhydrite assemblages also indicate multiple sulfatization stages in hydrothermal activities (Figure 7). Independent Ba-bearing minerals, e.g., barite and hyalophane, can be developed under sufficient Ba supply [46,62,63]. The enrichment of excess Ba in marine shale usually occurs under two conditions: high primary productivity and the significant impact of submarine hydrothermal activities on shale reservoirs.

Barite veins at the low-resistivity samples from Well N21 exhibit obvious positive Eu anomalies (1.71–1.83) compared with those at the normal resistivity shale samples (1.1 to 1.4), where Eu concentration is significantly lower than that at the Lower Cambrian Doushantuo barite [62–66]. Meanwhile, barite veins in the investigated low-resistivity samples are low in REE concentration (164.3 to 216.31 ppm) and Ce/La (0.8–2.5). The low total REE concentration suggests that their possible hydrothermal effects are similar to those reported from the Western Bastar Carton's continental rift margin [62]. Moreover, excess Ba ($Ba_{xs}$) is an important parameter to express Ba enrichment (the accumulation method is referred to [64–66]), while the determined $Ba_{xs}$ is weakly positive with an Eu anomaly (R2 = 0.38, n = 8). Importantly, interference from high Ba-containing compounds reminds us to be cautious when interpreting Eu abnormalities measured by ICP-MS [66]. However, Ba enrichment in samples with $Ba_{xs}$ > 10,000 ppm has no positive correlation with the Eu anomaly. Therefore, these evidences indicated that Ba in barite may be from seawater with hydrothermal activity ([65,67], Figure 12). Moreover, the $\delta^{34}S$ value of barites filling fractures of low-resistivity shale samples ranges from 19.8 ‰ to 24.6 ‰, lower than Early Silurian seawater [35]. Therefore, the $\delta^{34}S$‰ values of barites may be attributed to seawater mixed with hydrothermal fluids. The observed $\delta^{34}S$‰ range is similar to that from previous studies in other regions [62]. Consequently, the low-resistivity shale sulfate vein is more plausibly a result of either the inorganic reduction of marine sulfate or the inorganic fractionation of sulfur, likely triggered by hydrothermal activity [62].

#### 5.1.3. Feldspathisation Stage

Hyalophane, a tectosilicate mineral of the feldspar group, is commonly identified as a barium feldspar. It is typically observed in low- to medium-grade metamorphic, volcanic, or magmatic systems, where it can substitute for other feldspar minerals. It is frequently considered an indicator of hydrothermal activity [62,68] because of its co-existence with barium-enriched hydrothermal fluids. A comparison of hyalophane from the Longmaxi low-resistivity shale and typical hydrothermal fluids in the world shows that they are similar in major elements (Figure 14, [35,46,62,63,68]). The existence of hyalophane has been believed to be related to the hydrothermally induced diagenetic transformation of K-feldspar, based on previous investigations on the relationship between hyalophane and surrounding minerals in ore deposits [35,65]. For instance, Zan observed the close relationship between hyalophane, K-feldspar, and barite at nodules and black shales of the Longmaxi Formation in the Northern Sichuan Basin, and they hypothesized that K-feldspar had been largely replaced by hydrothermal $Ba^{2+}$ with the following reaction [65]:

$$2KAlSi_3O_{8\ (K\text{-feldspar})} + Ba^{2+} = (K, Ba)\ Al_2Si_2O_{8\ (hyalophane)} + 2\ K^+ + 4SiO_2. \quad (2)$$

This relationship between hyalophane, K-feldspar, and barite was also observed in our investigation, where K-feldspar is surrounded by hyalophane (Figure 7). Similarly, barite-containing hyalophane was also clearly detected in our samples, pointing to Ba-rich hydrothermal activity. These findings provide compelling evidence that the origin of hyalophane was closely associated with the infiltration of Ba-rich hydrothermal fluids into black shales, where they interacted with K-feldspar through various reactions. In addition, the massive hyalophane in this study with zonal structure was first discovered around low-resistivity shale veins. The outer zone is high in Ba content but low in K content, suggesting that the barium concentration was changed from low to high during hyalophane development. It confirms episodic activities occurring in barium-rich fluids in low-resistivity shales, which is also evidence of episodic activities in hydrothermal fluids under the control of faults [61].

#### 5.1.4. Calcitization Stage

The late-stage hydrothermal activity is distinguished by the widespread presence of calcite. Calcite (quartz) veins and calcite (quartz) chlorite veins crosscut various lithologies (Figure 7i). Limited microfractures and hydrothermal alterations are discernible in the

vicinity of the calcite-bearing veins [69–71]. The calcite veins in the low-resistivity shale of the Changning Block are mainly developed in two phases. The first phase might be derived from marine carbonate rocks, while the second phase is related to mixed fluids. The mixed fluids were mainly sourced from low-temperature hydrothermal fluids and hydrocarbon pyrolysis (Figure 13a,b). The calcite vein source is similar to that proposed by Wu [56].

Furthermore, the first phase is widespread at calcite veins in all shale samples from the Changning Block, with oxygen isotopes higher than −10‰, indicating calcite is slightly influenced by external fluids. The second phase is related to low-temperature hydrothermal fluids and is widespread in low-resistivity shale. An oxygen isotope lower than −10‰ indicates that calcite is strongly altered and reformed by fluids. The calcite veins from surrounding rock are rich in Al, Mg, and Fe but poor in Mn, while those from low-temperature hydrothermal fluids are rich in Mn, Fe, and Mg but poor in Al (Figure 13c,d). Calcite veins in low-resistivity shales were developed from low-temperature hydrothermal fluids interacting with rocks in a closed hydrocarbon-water-rock system. The Al-Fe-Mn ternary diagram indicates that the system was relatively closed, with minor hydrothermal fluid influence and no distal fluid influx. The mass fraction of Mn in acidic, neutral, and basic igneous rocks is $600 \times 10^{-6}$–$800 \times 10^{-6}$, $1200 \times 10^{-6}$–$1500 \times 10^{-6}$, and $1500 \times 10^{-6}$–$2500 \times 10^{-6}$, respectively. The mass fraction of Mn in atmospheric and seawater is low (generally less than $0.1 \times 10^{-6}$). Therefore, the Mn element in the calcite veins may have originated from magma-related hydrothermal fluids. However, the calcite formation related to hydrothermal fluids cannot be solely attributed to cooling. Precipitation of calcite from hydrothermal fluids typically occurs under various mechanisms, including (a) different fluid mixing, (b) $CO_2$ degassing, and (c) fluid-rock interaction [72]. It is apparent that calcite precipitation might result from fluid–rock interaction. Cation exchange and/or redox reactions can occur during interactions between high-temperature hydrothermal fluids and cooler wall rocks. This process involves $H^+$ ion loss from fluid and cation acquisition, e.g., $Na^+$, $Ca^{2+}$, $Mg^{2+}$, and $Fe^{2+}$. The reduction in $H^+$ ions increases fluid pH, ultimately leading to calcite crystallization [72]. Large-scale heating involving mantle plumes rising to the continental lithosphere in the late Permian brought a large amount of metal elements ($Mg^{2+}$, $Ca^{2+}$, and $Mn^{2+}$) related to intermediate-basic igneous rocks to formation water. Meanwhile, mixed $CO_2$, $H_2S$, and other gases escaping from basalt overflow can form a high-temperature hydrothermal mixed fluid. Upward migration of these hydrothermal fluids under high pressure compressed surrounding rocks to produce fractures, which precipitated in fractures to form calcite veins and anhydrite veins [56].

### *5.2. Graphitization of Organic Matter*

Organic matter in low-resistivity shale samples with hydrothermal fine veins is commonly at a higher thermal maturity stage compared with those without hydrothermal fine veins (Figures 5 and 6). The 508 organic matter samples from low-resistivity shale samples with hydrothermal fine veins have an average Ro value of 3.82%, while the 420 organic matter samples without hydrothermal fine veins have an average Ro value of 3.38%. Previous investigations have documented significant variation in the chemical structure of kerogen at a Ro of 3.5%, representing a critical turning point. Hence, a sharp increase in overall orderliness and crystallinity can occur in carbon atom layers, where the distance between carbon layers can be gradually decreased as organic matter structure transforms from amorphous carbon to crystalline graphite [58]. Meanwhile, the Raman spectra of FV samples also show obvious graphitization. In terms of low-resistivity shale with Ro higher than 3.5%, the ratio of graphite content to total organic matter content is higher than 25%, with high Dh/Gh values and an obvious Peak G′ (graphite peak) at Raman spectra [7]. The Dh/Gh values of 23 organic matter samples in FV range from 0.72 to 0.84, with an average of 0.74 (Figure 5a–d). In contrast, organic matter in NFV samples is poorly graphitized. For example, Dh/Gh values of OMs in Sample 3946.01 and Sample 3946.53 from Well NX2 are 0.56 and 0.59, respectively, with no obvious graphite peak (‘peak G) at Raman spectra, indicating that these samples have not undergone graphitization [7]. The widespread

graphitization of pyrobitumen and solid kerogen in low-resistivity shale may be related to hydrothermal reformation. Organic matter in low-resistivity shales is dominated by pyrobitumen and solid kerogen, with Ro higher than 3.5%, much higher than the maturity stage described by the classical hydrocarbon generation model [15]. Hydrothermal reformation can accelerate the graphitization of pyrobitumen and solid kerogen [15]. During this period, free electron flow in shale reservoirs increases with aromatized hydrocarbons, resulting in ordered carbon atoms and graphitized structures [3]. The aromatic cluster OM is gradually structured with increasing graphitization, and alpha bonds between carbon atoms are also progressively growing.

### *5.3. Hydrothermal Circulation*

In summary, this study demonstrates the low-temperature hydrothermal system evolution in the Changing Block, from the chlorite stage (150–180 °C) to the low-sulfidation stage (120–150 °C) and finally to the low-temperature calcitization stage. The high Mn content in hydrothermal calcite veins suggests that hydrothermal fluids came from magmatic sources. It is likely that metals were transported as chloride complexes in aqueous solutions. Migration of low-temperature hydrothermal fluids can heat rocks to increase formation temperature, thereby increasing the thermal maturity of shale and graphite content.

The Western Yangtze Block underwent eastward subduction of the Paleotethys Ocean's Ailaoshan slab in the early Guadalupe (269 Ma), which altered the nearby Emeishan mantle plume with recycled fragments of lithospheric materials. The southern Sichuan Basin was far from the Emeishan mantle plume at the end of the Guadalupian (260–257 Ma) when the lithosphere mantle was down thrusting in the Yangtze Continent [69–74]. The faults at the Paleozoic basement were reactivated during the late Permian, when hydrothermal fluids from formation water and seawater seeped down along fault systems and fracture systems at the Paleozoic basement to the deep crust under gravity. After that, a long-term water–rock reaction occurred at basement rocks, where $Mg^{2+}$, $Ca^{2+}$, $Mn^{2+}$, $Fe^{2+}$, and $Ba^{2+}$ ions were extracted from surrounding rocks. Additionally, volatile gases, e.g., $CO_2$ and $H_2S$, were mixed under high temperature and low pressure with the overflow of Emeishan basalt to form alkaline hot brine. The alkaline, hot brine expanded in volume with increasing temperature, developing high pore fluid pressure. As a result, it migrated upward along faults at the Paleozoic basement in the Tiangongtang and Shuanglong Luochang areas, rapidly increasing formation temperature and enhancing the thermal maturity of organic matter at the Wufeng–Longmaxi shale. Hydrothermal fluids generated fractures in shale rocks under high-pressure compression, where cation exchange and/or redox reactions occurred during the interaction of high-temperature hydrothermal fluid with cool wall rocks. The alkaline hot brine reactivated the water–rock reaction at the Wufeng–Longmaxi shale during migration, thus developing hydrothermal mineral assemblages filling in fractures, e.g., brunsvigite, barite, hyalophane, and anhydrite. Therefore, rapid increases in formation temperature accelerated the graphitization of organic matter, decreasing the resistivity of shale significantly. However, faults at the wings of the Changning anticline were well sealed, and the faults at the Paleozoic basement were not developed at that period, resulting in moderate or weak fluid activities and no cross-layer migration [69–74].

### *5.4. Impact of Hydrothermal Activities and Fault Systems on Electric Resistivity of Shales*

Generally, the distribution of low-resistivity shale with a resistivity < 5 Ω•m in Changning Block is directly controlled by the Paleozoic fault system and the late Permian hydrothermal fluids. The hydrothermal activities exerted an important impact on the thermal maturation and graphitization of organic matter in low-resistivity shale. They evolved Wufeng–Longmaxi shale from a mature one to an over-mature one, enhancing graphitization and decreasing organic pore volume in samples with hydrothermal modification.

The modification of low-temperature hydrothermal activities has a certain influence on organic pore development. Organic matter wrapped by hydrothermal minerals is at an over maturity stage (average Ro value: 3.82%) and is generally graphitized with an almost no c with a size of 2 nm to 53 nm (Figure 6). However, organic matters in samples at similar depth with hydrothermal fine veins have an average Ro value of 3.38%, where organic pores can be observed, with an average pore size of 823 nm (Figure 6). It is indicated that the graphitization considerably damaged OM pores and pore systems at shale reservoirs, which further widens the gap between low-resistivity shale and normal-resistivity shale because OM pores are the most important storage spaces for organic-rich shale [5]. This explains why organic matter wrapped by hydrothermal minerals is at a high maturity stage (the average Ro value is 3.82%), but few organic pores have developed (Figure 6a–d).

Therefore, hydrothermal fluids rapidly enhanced the thermal maturity of organic matter to 2.5%–3.5%, while OM pores were regularly deformed and collapsed when exposed to compaction or tectonics [2,11]. Shale resistivity has continued to decrease after rapidly entering the graphitization stage (Ro value: 3.5%–4.0%). As a result, the graphitization caused a rapid decrease in organic pores in kerogen and pyrobitumen. The existence of graphite in shale reservoirs, which is altered by igneous-associated hydrothermal fluids, has been reported to decrease rock resistivity and porosity [4]. Rasmussen and Fletcher reported that the dolerite sill that was intruded into shales in Western Australia together with alkaline hydrothermal fluids produced a coarse coke mosaic matrix, which was a sign of rapid heating in contact aureole [73]. Inferring that significant concentrations of graphite generated by hydrothermal fluid are present, high conductivity regions and underdeveloped organic pores in shale may be indicative of such areas.

Apart from the hydrothermal reformation at a late stage, the difference in preservation conditions at the Changning Block is also an important factor controlling low-resistivity shale distribution (Figure 17). Currently, some scholars have reported that cross-layer fluid activities were weak in the Changning anticline; however, fluid activities within layers were intense based on the study of strontium, carbon, and oxygen isotopes (Figure 14). Moreover, obvious isotopic endogeneity indicates that shale gas in the Changning anticline is well preserved, where low-resistivity shale is not developed [57]. Different from the Changning anticline, calcite veins in shales from NX2, N23, and N21 well blocks have different $^{87}Sr/^{86}Sr$ ratios with surrounding rocks. The difference of 0.001–0.003 indicates the occurrence of external fluid reformation. Uplifting occurred during the early Paleozoic to early Mesozoic, resulting in denudation and extension as well as the development of a large number of normal faults in the Tiangongtang, Shuanglong-Luochang, and Xuyong areas. A positive inversion structure was developed due to initial compression from the end of the Permian to the Triassic. After that, three phases of compressional deformation were superimposed from the middle Mesozoic to the Cenozoic, where fault systems in the Early Paleozoic further cut the Lower Paleozoic. As a result, the preservation conditions of the Wufeng–Longmaxi shale were strongly destroyed, decreasing resistivity in shale systems greatly. Meanwhile, these large faults acted as migration pathways for hydrothermal fluids during the late Permian to Triassic, increasing thermal maturity significantly. As a result, graphitization occurred in most organic matter to decrease the resistivity of shale reservoirs. For example, low-resistivity shale at Wells N22 and N21 is distributed to the east of the Huayingshan fault, and low-resistivity shale in the N23 well block is developed near the Yanjin-Gulin basement faults (Figure 17). The low-resistivity shale near Paleozoic faults is characterized by low resistivity (0.01–5.02 Ω•m), high thermal maturity (Ro of 3.62%–3.94%), and significant graphitization (>25%) [5,6,32].

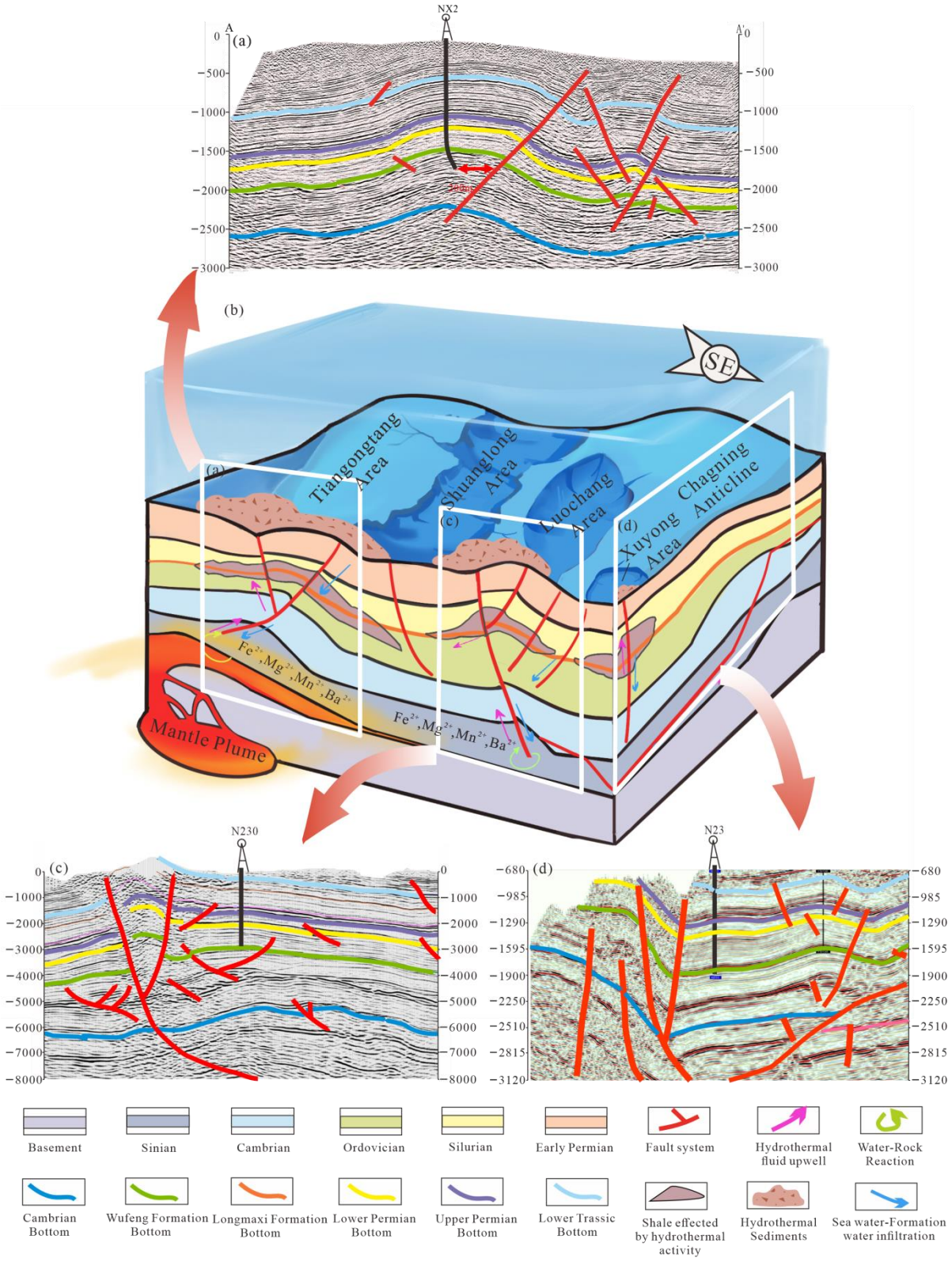


**Figure 17.** Model of control of low-temperature hydrothermal events and Paleozoic basement fault systems on low-resistivity shale reservoirs at the Changning Block. (**a**) NX2 well is located beside the Paleozoic basement fault systems in the Tiangongtang Area. (**b**) Model of Paleozoic fault systems and later Permian hydrothermal activities controlling graphitization of low-resistivity shale at the Changning Block. (**c**) N230 well and the Huayingshan fault are close to each other in the Shuanglong-Luochang Area. (**d**) N230 well is close to the Yanjin-Gulin basement fault system.

## 6. Conclusions

Underestimating low resistivity and low contrast pay zones in shale has historically missed opportunities for shale oil and gas exploration and production. Highly graphitized and low-resistivity shale is commonly characterized by poor reservoir quality, making it challenging to seek subsequent shale oil and gas targets. Understanding the origin of organic matter graphitization is crucial for effective shale gas and oil exploration and exploitation in the Southern Sichuan Basin.

The low-resistivity shale at the Changning Block, with an average resistivity <5 Ω•m, has been observed to frequently develop fine vein structures filled by hydrothermal minerals. The most common hydrothermal minerals include brunsvigite, barite-hyalophane-barium, feldspar-potassium feldspar-anhydrite, and calcite-ankerite. The small-scale hydrothermal heating at the P-T transition is one of the reasons for the rapid increase in thermal maturity and graphitization of low-resistivity shale at the Changning Block.

Hydrothermal activities exert a significant influence on the thermal maturity and graphitization of organic matter in low-resistivity shale. It is notably confirmed by three pieces of evidence: (a) evolving shale from a mature one or over a mature one; (b) enhancing graphitization of shale reservoirs; and (c) reducing organic pore volume in samples subjected to hydrothermal modification. The low-resistivity shale with well-developed hydrothermal fine veins has 3.82% Ro values, with graphitization up to 25%. The maturity of organic matter rapidly increases to 2.5%–3.5% under heating by hydrothermal fluids. Meanwhile, the low-resistivity shale experiences intense mechanical compaction, decreasing porosity slightly. The shale resistivity continues to decrease after entering the graphitization stage, where organic pores generated by graphitization are rapidly reduced in number.

The distribution of the low-resistivity shale with a resistivity <5 Ω•m at the Changning Block and the graphitization are directly controlled by Paleozoic fault systems and hydrothermal fluids associated with the later Permian Emeishan mantle plume. Formation water and sea water were penetrated into the deep crust along the Paleozoic basement fault and fracture systems under gravity, where they were heated by the mantle plume to generate a series of water-rock reactions at basement rocks. As a result, $Mg^{2+}$, $Ca^{2+}$, $Mn^{2+}$, $Fe^{2+}$, and $Ba^{2+}$ ions were extracted to form alkaline hot brine that was migrated upward along Paleozoic basement faults in Tiangongtang, Shuanglong-Luochang, and Xuyong areas, rapidly increasing formation temperature and enhancing maturation and graphitization of organic matter in Wufeng–Longmaxi shale. As a result, shale resistivity was significantly decreased.

**Author Contributions:** Conceptualization, T.Z. and Q.Z.; methodology, S.M and Z.S.; software, W.G., J.G. and F.C.; validation, P.L.; formal analysis, J.C. and S.M.; investigation, S.S. and L.Q.; resources, Z.S.; data curation, H.W.; writing—original draft preparation, T.Z.; writing—review and editing, T.Z.; supervision, Q.Z.; project administration, H.W.; funding acquisition, S.S. All authors have read and agreed to the published version of the manuscript.

**Funding:** This research received no external funding.

**Data Availability Statement:** Data is unavailable due to privacy or ethical restrictions.

**Conflicts of Interest:** The authors declare no conflict of interest.

## References

1. Ashqar, A.; Uchida, M.; Salahuddin, A.A.; Olayiwola, S.O.; Awolayo, A.N. Evaluating a Complex Low-Resistivity Pay Carbonate Reservoir Onshore Abu Dhabi: From Model to Implementation. In Proceedings of the International Petroleum Exhibition & Conference, Abu Dhabi, United Arab Emirates, 14 November 2016; University of Calgary: Abu Dhabi, United Arab Emirates, 2016.
2. Loukola-Ruskeeniemi, K.; Hyvönen, E.; Airo, M.; Lerssi, J.; Arkimaa, H. Country-wide exploration for graphite- and sulphide-rich black shales with airborne geophysics and petrophysical and geochemical studies. *J. Geochem. Explor.* **2023**, *244*, 107123. [CrossRef]
3. Xue, Z.; Jiang, Z.; Wang, X.; Gao, Z.; Chang, J.; Nie, Z.; Li, H.; Wu, W.; Qiu, H.; Wang, Q.; et al. Genetic mechanism of low resistivity in high-mature marine shale: Insights from the study on pore structure and organic matter graphitization. *Mar. Petrol. Geol.* **2022**, *144*, 105825. [CrossRef]

4. Spacapan, J.B.; D Odorico, A.; Palma, O.; Galland, O.; Senger, K.; Ruiz, R.; Manceda, R.; Leanza, H.A. Low resistivity zones at contacts of igneous intrusions emplaced in organic-rich formations and their implications on fluid flow and petroleum systems: A case study in the northern Neuquén Basin, Argentina. *Basin Res.* **2019**, *32*, 3–24. [CrossRef]
5. Wang, Y.; Wei, G.; Shen, J.; Qiu, Z.; Li, X.; Zhang, Q.; Zhang, L.; Wang, C.; Liu, W. Analysis on distribution and main controlling factors of OM carbonization in marine shale in the Sichuan Basin of China and its periphery. *J. Nat. Gas Geosci.* **2022**, *7*, 181–197. [CrossRef]
6. Cao, T.; Deng, M.; Cao, Q.; Huang, Y.; Yu, Y.; Cao, X. Pore formation and evolution of organic-rich shale during the entire hydrocarbon generation process: Examination of artificially and naturally matured samples. *J. Nat. Gas Sci. Eng.* **2021**, *93*, 104020. [CrossRef]
7. Ma, X.; Wang, H.; Zhou, T.; Zhao, Q.; Shi, Z.; Sun, S.; Cheng, F. Geological Controlling Factors of Low Resistivity Shale and Their Implications on Reservoir Quality: A Case Study in the Southern Sichuan Basin, China. *Energies* **2022**, *15*, 5801. [CrossRef]
8. Tang, X.; Jiang, S.; Jiang, Z.; Li, Z.; He, Z.; Long, S.; Zhu, D. Heterogeneity of Paleozoic Wufeng-Longmaxi formation shale and its effects on the shale gas accumulation in the Upper Yangtze Region, China. *Fuel* **2019**, *239*, 387–402. [CrossRef]
9. Yan, W.; Sun, J.; Zhang, J.; Yuan, W.; Zhang, L.; Cui, L.; Dong, H. Studies of electrical properties of low-resistivity sandstones based on digital rock technology. *J. Geophys. Eng.* **2018**, *15*, 153–163. [CrossRef]
10. Jianmeng, S.; Zhu, X.; Hong, L.; Hongpan, Z.; Jinjiang, Z.; Aarnes, I.; Aarnes, I. Mechanism analysis and logging evaluation of low resistivity in lower Paleozoic shale gas reservoirs of Yangtze region. *J. China Univ. Pet.* **2018**, *42*, 47–56.
11. Xu, S.; Yassin, M.R.; Dehghanpour, H.; Kolbeck, C. The effects of kerogen maturity on pore structure and wettability of organic-rich calcareous shales. *J. Mol. Liq.* **2022**, *362*, 119577. [CrossRef]
12. Senger, K.; Birchall, T.; Betlem, P.; Ogata, K.; Ohm, S.; Olaussen, S.; Paulsen, R.S. Resistivity of reservoir sandstones and organic rich shales on the Barents Shelf: Implications for interpreting CSEM data. *Geosci. Front.* **2021**, *12*, 101063. [CrossRef]
13. Li, Y.; Li, M.; Zhang, J.; Pang, Q.; Zou, C.; Shu, H.; Wang, G. Influence of the Emeishan basalt eruption on shale gas enrichment: A case study of shale from Wufeng-Longmaxi formations in northern Yunnan and Guizhou provinces. *Fuel* **2020**, *282*, 118835. [CrossRef]
14. Passos, A.S.D.; Dessuy, M.B.; Nakadi, F.V.; de Andrade, J.B.; Vale, M.G.R. Investigation of different chemical modifiers based on the Pd/Mg mixture for the determination of sulfur in shale oil by high-resolution continuum source graphite furnace molecular absorption spectrometry. *Talanta* **2019**, *204*, 206–212. [CrossRef]
15. Hou, Y.; Zhang, K.; Wang, F.; He, S.; Dong, T.; Wang, C.; Qin, W.; Xiao, Y.; Tang, B.; Yu, R.; et al. Structural evolution of organic matter and implications for graphitization in over-mature marine shales, south China. *Mar. Petrol. Geol.* **2019**, *109*, 304–316. [CrossRef]
16. Liu, X.; Zhuo, Y.; Feng, M.; Zhang, B.; Xia, M.; Wang, X. Constrains of eruption environment and hydrothermal fluid on the Permian pyroclastic reservoirs in the Sichuan Basin, SW China. *Petroleum* **2022**, *8*, 17–30. [CrossRef]
17. Jerram, D.A.; Widdowson, M.; Wignall, P.B.; Sun, Y.; Lai, X.; Bond, D.P.G.; Torsvik, T.H. Submarine palaeoenvironments during Emeishan flood basalt volcanism, SW China: Implications for plume–lithosphere interaction during the Capitanian, Middle Permian ('end Guadalupian') extinction event. *Palaeogeogr. Palaeoclimatol. Palaeoecol.* **2016**, *441*, 65–73. [CrossRef]
18. Yuguang, H.; Kunpeng, Z.; Sheng, H.; Weifeng, T.; Yan, X.; Cheng, W.; Rui, Y. Origin and geological siginificance of ultrs-low resistivity in Lower Paleozoic marine shale, Southern China. *Geol. Scinece Technol.* **2021**, *40*, 80–89.
19. Yunfeng, Y.; Fang, B.; Geer, T.; Anyang, P.; Baojian, S. Characteristics of organic matter-hosted pores in Lower Silurian Longmaxi shale with different maturities, Sichuan Basin. *Pet. Geol. Exp.* **2020**, *42*, 387–397.
20. Gao, Z.; Fan, Y.; Xuan, Q.; Zheng, G. A review of shale pore structure evolution characteristics with increasing thermal maturities. *Adv. Geo-Energy Res.* **2020**, *4*, 247–259. [CrossRef]
21. Wang, R.; Hu, Z.; Long, S.; Liu, G.; Zhao, J.; Dong, L.; Du, W.; Wang, P.; Yin, S. Differential Characteristics of the Upper Ordovician-Lower Silurian Wufeng-Longmaxi Shale Reservoir and its Implications for Exploration and Development of Shale Gas in/around the Sichuan Basin. *Acta. Geol. Sin.* **2019**, *93*, 520–535. [CrossRef]
22. Yunfeng, Y. Application of bitumen and graptolite reflectance in the Silurian Longmaxi shale, southeastern Sichuan Basin. *Pet. Geol. Exp.* **2016**, *38*, 466–472.
23. Wang, R.; Gu, Y.; Ding, W.; Gong, D.; Yin, S.; Wang, X.; Zhou, X.; Li, A.; Xiao, Z.; Cui, Z. Characteristics and dominant controlling factors of organic-rich marine shales with high thermal maturity: A case study of the Lower Cambrian Niutitang Formation in the Cen'gong block, southern China. *J. Nat. Gas Sci. Eng.* **2016**, *33*, 81–96. [CrossRef]
24. Zhang, B.; Wen, H.; Qing, H.; Yang, K.; Luo, Y.; Yang, H.; Wang, P.; He, L.; Xiao, W. The influence of depositional and diagenetic processes on rock electrical properties: A case study of the Longmaxi shale in the Sichuan Basin. *J. Petrol. Sci. Eng.* **2022**, *211*, 110119. [CrossRef]
25. Wu, F.; Dai, J.; Wen, Z.; Yao, C.; Shi, X.; Liang, L.; Yun, L.; Shi, B. Resistivity anisotropy analysis of Longmaxi shale by resistivity measurements, scanning electron microscope, and resistivity simulation. *J. Appl. Geophys.* **2022**, *203*, 104700. [CrossRef]
26. Wang, Y.; Li, X.; Chen, B.; Wu, W.; Dong, D.; Zhang, J.; Han, J.; Ma, J.; Dai, B.; Wang, H.; et al. Lower limit of thermal maturity for the carbonization of organic matter in marine shale and its exploration risk. *Petrol. Explor. Dev.* **2018**, *45*, 402–411. [CrossRef]
27. Qiu, Z.; Liu, B.; Lu, B.; Shi, Z.; Li, Z. Mineralogical and petrographic characteristics of the Ordovician-Silurian Wufeng-Longmaxi Shale in the Sichuan Basin and implications for depositional conditions and diagenesis of black shales. *Mar. Petrol. Geol.* **2022**, *135*, 105428. [CrossRef]

28. Shi, Z.; Qiu, Z. Main Bedding Types of Marine Fine-Grained Sediments and their Significance for Oil and Gas Exploration and Development. *Acta. Sedimentol. Sin.* **2021**, *39*, 181–196.
29. Shi, Z.; Zhou, T.; Guo, W.; Liang, P.; Cheng, F. Quantitative Paleogeographic Mapping and Sedimentary Microfacies Division in a Deep-water Marine Shale Shelf: Case study of Wufeng-Longmaxi shale, southern Sichuan Basin, China. *Acta. Sedimentol. Sin.* **2022**, *40*, 17.
30. Hongyan, W.; Zhensheng, S.; Shasha, S.; Leifu, Z.; Aarnes, I. Characterization and genesis of deep shale reservoirs in the first Member of the Silurian Longmaxi Formation in southern Sichuan Basin and its periphery. *Oil Gas Geol.* **2021**, *42*, 66–75.
31. Shi, Z.; Zhou, T.; Wang, H.; Sun, S. Depositional Structures and Their Reservoir Characteristics in the Wufeng–Longmaxi Shale in Southern Sichuan Basin, China. *Energies* **2022**, *15*, 1618. [CrossRef]
32. Wang, Y.; Jia, H.; Kou, Y.; Hao, Z. Causes of low resistivity of Longmaxi Formation shale reservoirs in Changning area. *Pet. Geol. Recovery Effic.* **2021**, *19*, 53–61.
33. He, X.; Wu, J.; Yong, R.; Zhao, S. Hydrocarbon accumulation and key exploration & development technologies of Changning-Weiyuan marine shale gas field, southern Sichuan. *Pet. Res.* **2021**, *6*, 1–15.
34. Wang, X.; Zhang, B.; He, Z.; He, L.; Yang, K.; Huang, T.; Luo, F.; Tang, J.; Gan, L. Electrical properties of Longmaxi organic-rich shale and its potential applications to shale gas exploration and exploitation. *J. Nat. Gas Sci. Eng.* **2016**, *36*, 573–585. [CrossRef]
35. Zan, B.; Mou, C.; Lash, G.G.; Yan, J.; Hou, Q. Diagenetic barite-calcite-pyrite nodules in the Silurian Longmaxi Formation of the Yangtze Block, South China: A plausible record of sulfate-methane transition zone movements in ancient marine sediments. *Chem. Geol.* **2022**, *595*, 120789. [CrossRef]
36. Craddock, P.R.; Bach, W. Insights to magmatic–hydrothermal processes in the Manus back-arc basin as recorded by anhydrite. *Geochim. Cosmochim. Ac.* **2010**, *74*, 5514–5536. [CrossRef]
37. Žigaitė, Ž.; Qvarnström, M.; Bancroft, A.; Pérez-Huerta, A.; Blom, H.; Ahlberg, P.E. Trace and rare earth element compositions of Silurian conodonts from the Vesiku Bone Bed: Histological and palaeoenvironmental implications. *Palaeogeogr. Palaeoclimatol. Palaeoecol.* **2020**, *549*, 109449. [CrossRef]
38. Sun, S.S.; McDonough, W.F. Chemical and isotopic systematics of oceanic basalts: Implications for mantle composition and processes. *Geol. Soc. Lond. Spec. Publ.* **1989**, *42*, 313–345. [CrossRef]
39. Wille, G.; Schmidt, U.; Hollricher, O. RISE: Correlative Confocal Raman and Scanning Electron Microscopy. In *Confocal Raman Microscopy*; Springer International Publishing: Cham, Switzerland, 2018; pp. 559–580.
40. Tian, H.; Li, T.; Zhang, T.; Xiao, X. Characterization of methane adsorption on overmature Lower Silurian–Upper Ordovician shales in Sichuan Basin, southwest China: Experimental results and geological implications. *Int. J. Coal Geol.* **2016**, *156*, 36–49. [CrossRef]
41. Schoenherr, J.; Littke, R.; Urai, J.L.; Kukla, P.A.; Rawahi, Z. Polyphase thermal evolution in the Infra-Cambrian Ara Group (South Oman Salt Basin) as deduced by maturity of solid reservoir bitumen. *Org. Geochem.* **2007**, *38*, 1293–1318. [CrossRef]
42. Ducut, J.D.; Alipio, M.; Go, P.J.; Concepcion, R., II; Vicerra, R.R.; Bandala, A.; Dadios, E. A Review of Electrical Resistivity Tomography Applications in Underground Imaging and Object Detection. *Displays* **2022**, *73*, 102208. [CrossRef]
43. Zhang, S.; Yan, J.; Cai, J.; Zhu, X.; Hu, Q.; Wang, M.; Geng, B.; Zhong, G. Fracture characteristics and logging identification of lacustrine shale in the Jiyang Depression, Bohai Bay Basin, Eastern China. *Mar. Petrol. Geol.* **2021**, *132*, 105192. [CrossRef]
44. Wang, S.; Wang, G.; Huang, L.; Song, L.; Zhang, Y.; Li, D.; Huang, Y. Logging evaluation of lamina structure and reservoir quality in shale oil reservoir of Fengcheng Formation in Mahu Sag, China. *Mar. Petrol. Geol.* **2021**, *133*, 105299. [CrossRef]
45. Khoshbakht, F.; Azizzadeh, M.; Memarian, H.; Nourozi, G.H.; Moallemi, S.A. Comparison of electrical image log with core in a fractured carbonate reservoir. *J. Petrol. Sci. Eng.* **2012**, *86,87*, 289–296. [CrossRef]
46. Okubo, J.; Klyukin, Y.I.; Warren, L.V.; Sublett, D.M.; Bodnar, R.J.; Gill, B.C.; Xiao, S. Hydrothermal influence on barite precipitates in the basal Ediacaran Sete Lagoas cap dolostone, São Francisco Craton, central Brazil. *Precambrian Res.* **2020**, *340*, 105628. [CrossRef]
47. Kuhn, T.; Herzig, P.M.; Hannington, M.D.; Garbe-Schönberg, D.; Stoffers, P. Origin of fluids and anhydrite precipitation in the sediment-hosted Grimsey hydrothermal field north of Iceland. *Chem. Geol.* **2003**, *202*, 5–21. [CrossRef]
48. Zane, A.; Weiss, Z. A procedure for classifying rock-forming chlorites based on microprobe data. *Rend. Lincei.* **1998**, *9*, 51–56. [CrossRef]
49. Kranidiotis, P.; Maclean, W.H. Systematics of chlorite alteration at the Phelps Dodge massive sulfide deposit, Matagami, Quebec. *Econ. Geol.* **1987**, *82*, 1898–1911. [CrossRef]
50. Inoue, A.; Inoué, S.; Utada, M. Application of chlorite thermometry to estimation of formation temperature and redox conditions. *Clay Miner.* **2018**, *53*, 143–158. [CrossRef]
51. Taylor, S.R.; McLennan, S.M. *The Continental Crust: Its Composition and Evolution*; U.S. Department of Energy, Office of Scientific and Technical Information: Washington, DC, USA, 1985.
52. Adachi, M.; Yamamoto, K.; Sugisaki, R. Hydrothermal chert and associated siliceous rocks from the northern Pacific their geological significance as indication od ocean ridge activity. *Sediment Geol.* **1986**, *47*, 125–148. [CrossRef]
53. Yamamoto, K. Geochemical characteristics and depositional environments of cherts and associated rocks in the Franciscan and Shimanto Terranes. *Sediment Geol.* **1987**, *52*, 65–108. [CrossRef]

54. Arbiol, C.; Layne, G.D.; Zanoni, G.; Šegvić, B. Characteristics and genesis of phyllosilicate hydrothermal assemblages from Neoproterozoic epithermal Au-Ag mineralization of the Avalon Zone of Newfoundland, Canada. *Appl. Clay Sci.* **2021**, *202*, 105960. [CrossRef]
55. Worden, R.H.; Griffiths, J.; Wooldridge, L.J.; Utley, J.E.P.; Lawan, A.Y.; Muhammed, D.D.; Simon, N.; Armitage, P.J. Chlorite in sandstones. *Earth-Sci. Rev.* **2020**, *204*, 103105. [CrossRef]
56. Wu, A.; Cao, J.; Zhang, J. Bedding-parallel calcite veins indicate hydrocarbon–water–rock interactions in the over-mature Longmaxi shales, Sichuan Basin. *Mar. Petrol. Geol.* **2021**, *133*, 105303. [CrossRef]
57. Sun, B. Characteristics of Structural Deformation and Fluid Activity in Changning Area and Its' Perphery, Southern Sichuan. Master's Thesis, Chengdu University of Technology, Chengdu, China, 2018.
58. Delle Piane, C.; Ansari, H.; Li, Z.; Mata, J.; Rickard, W.; Pini, R.; Dewhurst, D.N.; Sherwood, N. Influence of organic matter type on porosity development in the Wufeng-Longmaxi Shale: A combined microscopy, neutron scattering and physisorption approach. *Int. J. Coal Geol.* **2022**, *249*, 103880. [CrossRef]
59. Chu, G.; Zhang, S.; Zhang, X.; Xiao, B.; Han, J.; Zhang, Y.; Cheng, J.; Feng, Y. Chlorite chemistry of Tongshankou porphyry-related Cu–Mo–W skarn deposit, Eastern China: Implications for hydrothermal fluid evolution and exploration vectoring to concealed orebodies. *Ore Geol. Rev.* **2020**, *122*, 103531. [CrossRef]
60. Wei, W.; Chen, X.; Yu, Z.; Chen, W.; Fang, Q.; Tang, X.; Ling, H. Different hydrothermal fluids inducing alteration and uranium mineralisation in the Baquan deposit of the Xiangshan uranium ore field: Constraints from geochemistry of altered rocks and ores. *Ore Geol. Rev.* **2021**, *139*, 104475. [CrossRef]
61. Han, G.; Wang, L.; Xiao, D.; Lou, D.; Xu, M.; Zhao, Y.; Pei, Y.; Guo, X.; Teng, J.; Han, Y. Magmatic hydrothermal fluid genesis of zeolite in the Paleogene Kongdian Formation of Zaoyuan oilfield, Bohai Bay Basin, China. *Petrol. Explor. Dev.* **2021**, *48*, 1101–1112. [CrossRef]
62. Dora, M.L.; Roy, S.K.; Khan, M.; Randive, K.; Kanungo, D.R.; Barik, R.; Kaushik, C.S.; Bari, S.H.; Pattanayak, R.S.; Krishna, K.V.S.; et al. Rift-induced structurally controlled hydrothermal barite veins in 1.6 Ga granite, Western Bastar Craton, Central India: Constraints from fluid inclusions, REE geochemistry, sulfur and strontium isotopes studies. *Ore Geol. Rev.* **2022**, *148*, 105050. [CrossRef]
63. Dekov, V.M.; Kyono, K.; Yasukawa, K.; Guéguen, B.; Ivarsson, M.; Kamenov, G.D.; Yamanaka, T.; Asael, D.; Ishida, M.; Cavalcante, L.L.; et al. Mineralogy, geochemistry and microbiology insights into precipitation of stibnite and orpiment at the Daiyon-Yonaguni Knoll (Okinawa Trough) hydrothermal barite deposits. *Chem. Geol.* **2022**, *610*, 121092. [CrossRef]
64. Schoepfer, S.D.; Shen, J.; Wei, H.; Tyson, R.V.; Ingall, E.; Algeo, T.J. Total organic carbon, organic phosphorus, and biogenic barium fluxes as proxies for paleomarine productivity. *Earth-Sci. Rev.* **2015**, *149*, 23–52. [CrossRef]
65. Wu, Y.; Tian, H.; Dong, D.; Li, T.; Zhou, Q. Paleo-environmental variation and its control on organic matter enrichment of black shales from shallow shelf to slope regions on the Upper Yangtze Platform during Cambrian Stage 3. *Palaeogeogr. Palaeoclimatol. Palaeoecol.* **2020**, *545*, 109653. [CrossRef]
66. Dulski, P. Interferences of oxide, hydroxide and chloride analyte species in the determination of rare earth elements in geological samples by inductively coupled plasma-mass spectrometry. *Fresenius J. Anal. Chem.* **1994**, *350*, 194–203. [CrossRef]
67. Barrett, T.J.; Jarvis, I.; Jarvis, K.E. Rare earth element geochemistry of massive sulfides-sulfates and gossans on the Southern Explorer Ridge. *Geology* **1990**, *18*, 583–586. [CrossRef]
68. Zhou, Z.; Wen, H.; Qin, C.; de Fourestier, J.; Liu, L.; Shi, Q. The genesis of the Dahebian Zn-Pb deposit and associated barite mineralization: Implications for hydrothermal fluid venting events along the Nanhua Basin, South China. *Ore Geol. Rev.* **2018**, *101*, 785–802. [CrossRef]
69. Melekestseva, I.Y.; Tret'Yakov, G.A.; Nimis, P.; Yuminov, A.M.; Maslennikov, V.V.; Maslennikova, S.P.; Kotlyarov, V.A.; Beltenev, V.E.; Danyushevsky, L.V.; Large, R. Barite-rich massive sulfides from the Semenov-1 hydrothermal field (Mid-Atlantic Ridge, 13°30.87′ N): Evidence for phase separation and magmatic input. *Mar. Geol.* **2014**, *349*, 37–54. [CrossRef]
70. Jamieson, J.W.; Hannington, M.D.; Tivey, M.K.; Hansteen, T.; Williamson, N.M.B.; Stewart, M.; Fietzke, J.; Butterfield, D.; Frische, M.; Allen, L.; et al. Precipitation and growth of barite within hydrothermal vent deposits from the Endeavour Segment, Juan de Fuca Ridge. *Geochim. Cosmochim. Ac.* **2016**, *173*, 64–85. [CrossRef]
71. Li, C.; Shen, P.; Li, P.; Sun, J.; Feng, H.; Pan, H. Changes in the factors controlling the chlorite composition and their influence on hydrothermal deposit studies: A case study from Hongguleleng Manto-type Cu deposit. *J. Geochem. Explor.* **2022**, *243*, 107096. [CrossRef]
72. Qaim Raza, M.; Absar, N.; Pandalai, H.S.; Patel, S.C. Chlorite thermometry and fluid inclusion studies on vein-type Tintini copper deposit, Eastern Dharwar Craton, India: Ore genetic implications. *Ore Geol. Rev.* **2021**, *131*, 104058. [CrossRef]

73. Rasmussen, B.; Fletcher, I.R. Indirect dating of mafic intrusions by SHRIMP U-Pb analysis of monazite in contact metamorphosed shale: An example from the Palaeoproterozoic Capricorn Orogen, Western Australia. *Earth Planet. Sci. Lett.* **2002**, *197*, 287–299. [CrossRef]
74. Meng, F.; Tian, Y.; Kerr, A.C.; Wang, W.; Wu, Z.; Xu, Q.; Du, Q.; Zhou, Y.; Liu, J. Geochemistry and petrogenesis of Late Permian basalts from the Sichuan Basin, SW China: Implications for the geodynamics of the Emeishan mantle plume. *J. Asian Earth Sci.* **2023**, *241*, 105477. [CrossRef]